UNIVERSITY OF CALIFORNIA SAN DIEGO

Biocompatibility and Delivery of a Hydrogel Barrier for the Prevention of Postsurgical Cardiac Adhesions

A Thesis submitted in partial satisfaction of the requirements

for the degree of Master of Science

in

Bioengineering

by

Austin John Burdick

Committee in charge:

Professor Karen Christman, Chair
Professor Michael Madani
Professor Jeff Omens

2018

The thesis of Austin John Burdick is approved, and it is acceptable in quality and form for publication on microfilm and electronically:

_____

_____

_____

Chair

University of California San Diego

2018

DEDICATION

To my family

TABLE OF CONTENTS

LIST OF ABBREVIATIONS

PMC, pericardial mesothilial cell

KGF, keratinocyte growth factor

ECM, extracellular matrix

PEG, poly(ethylene glycol)

PLA, poly(lactic acid)

PEG-Ald, poly(ethylene glycol)-aldehyde

PEG-AO, poly(ethylene glycol)-aminooxy

PEG-NPC, poly(ethylene glycol)- 4 - nitrophenyl chloroformate

PEG-DOPA, poly(ethylene glycol)-dopamine

Ald-AO, poly(ethylene glycol)-aldehyde and poly(ethylene glycol)-aminooxy hydrogel

Ald-AO-DOPA, poly(ethylene glycol)-aldehyde, poly(ethylene glycol)-aminooxy, and poly(ethylene glycol)-dopamine hydrogel

PBS, phosphate-buffered saline

DPBS, Dulbecco's phosphate-buffered saline

HNE, 4-hydroxynonenal

MDA, malondialdehyde

DCM, dichloromethane

NPC, 4 - nitrophenyl chloroformate

NMP, 1-methyl-2-pyrrolidone

TEA, trimethylamine

DOPA, dopamine hydrochloride

PEG-NPC, poly(ethylene glycol)- nitrophenylchloroformate

NMR, nuclear magnetic resonance

EDAC, N-(3-Dimethylaminopropyl)-N'ethylcarbodiimide hydrochloride

PEG-HPT, poly(ethylene glycol)-hydroxyphthalimide

THF, tetrahydrofuran

DMEM, Dulbecco's modified eagle's medium

FBS, fetal bovine serum

P/S, penicillin/streptomycin

AA, ascorbic acid

GSH, glutathione

ANOVA, analysis of variance

FTIR, Fourier transform infrared spectroscopy

LIST OF SYMBOLS

P_1, initial pressure

Q_1, initial air flow

P_2, final pressure

Q_2, final air flow

v_{max}, maximum velocity

v_{ave}, average velocity

v, velocity

p, pressure

t, time

F, force

μ, viscosity

ρ, density

k, turbulent kinetic energy

$\mathcal{E}$, dissipation rate of turbulent kinetic energy

σ_k, Prandtl number for turbulent kinetic energy

σ_ε, Prandtl number for the dissipation rate of turbulent kinetic energy

C_2, experimental constant

G_k, generation of turbulent kinetic energy

Y_M, fluid compressibility factor

S_k, user-defined generation of turbulent kinetic energy

S_ε, user-defined generation of dissipation of turbulent kinetic energy

μ_t, eddy viscosity

S, mean rate-of-strain tensor

$\overrightarrow{v_p}$, particle velocity vector

$\vec{v}$, fluid velocity vector

ρ_p, particle density

ρ_f, fluid density

$\vec{F}$, force vector

I, moment of inertia

d_p, particle diameter

M, Magnus lift force

C_r, rotational lift coefficient

$\vec{V}$, relative particle velocity

A, particle surface area

S_p, spin parameter

$\overrightarrow{\omega_0}$, relative angular velocity

v_{inj1}, injection velocity of Design 1

$v_{inj2,}$ injection velocity of Design 2

$\dot{m}_{AO1}$, mass flux of PEG-AO in Design 1

$\dot{m}_{AO2}$, mass flux of PEG-DOPA in Design 1

$\dot{m}_{DOPA1}$, mass flux of PEG-AO in Design 2

$\dot{m}_{DOPA2}$, mass flux of PEG-DOPA in Design 2

Re_{hd}, hydraulic diameter Reynolds number

d_{hd}, hydraulic diameter

κ_{air}, kinematic viscosity of air

Re_{hd1}, hydraulic diameter Reynolds number for Design 1

Re_{hd2}, hydraulic diameter Reynolds number for Design 2

T, turbulence intensity

T_1, turbulence intensity at Design 1 inlet

T_2, turbulence intensity at Design 2 inlet

LIST OF FIGURES

LIST OF TABLES

LIST OF GRAPHS

ACKNOWLEDGMENTS

I would like to thank Professor Karen Christman, my committee chair, for her guidance and for giving me the opportunity to work on this project within her lab. I also want to acknowledge my other committee members, Professor Michael Madani and Professor Jeff Omens, for their assistance during this research. Lastly, I want to thank Dr. Gina Policastro for her additional mentorship and support throughout this past year, as well as all of my colleagues in the Christman lab.

ABSTRACT OF THE THESIS

Biocompatibility and Delivery of a Hydrogel Barrier for the Prevention of Postsurgical Cardiac Adhesions

by

Austin John Burdick

Master of Science in Bioengineering

University of California San Diego, 2018

Professor Karen Christman, Chair

Previous research into the problem of postsurgical cardiac adhesions has produced a hydrogel barrier that can be applied to the surface of the heart, preventing the formation of adhesions in the weeks following trauma during surgery. When developing this type of gel for clinical translation, two issues that must be addressed are the biocompatibility of the material as well as a method of hydrogel delivery to the tissue surface. Previous research yielded a hydrogel made from poly(ethylene glycol) functionalized with aldehyde, aminooxy and dopamine groups. Cell viability is reduced in culture treated with this material due to the inclusion of dopamine. Examination of the hydrogel in culture through fluorescence microscopy and spectrophotometry

indicate that this is primarily due to oxidative stress, demonstrated by increased levels of hydrogen peroxide and lipid peroxidation. However, metabolic and morphological assays performed *in vitro* demonstrate that the biological antioxidant glutathione, a mediator of dopamine effects, can maintain cell viability when added as a culture supplement. Within this study, the effective application of the gel is achieved through air-assisted liquid spray, which allows equal distribution of two separate polymer solutions onto the surface of the heart. This result is predicted computationally through simulation of separate intersecting sprays and verified by spectroscopy and rheological testing of the material produced by a novel device. By investigating these factors, better understanding of the material's biological properties and implementation can be obtained to guide future research.

Chapter 1:

Introduction

Introduction

Cardiothoracic surgery is a procedure that has proven vital for a significant number of patients in the world today. During the past decade, the Society of Thoracic Surgeons reported an average of over 250,000 cardiac procedures in adults alone within the United States (STS 2017, 2–6). These include several distinct modes of treatment for cardiovascular ailments, including coronary artery bypass grafting as well as mitral and aortic valve replacement and repair (STS 2017, 2–6). Even after initial procedures, however, reoperations are common among patients years later and can result in further complications such as tissue damage and hemorrhage during reentry (Cannata et al. 2013, 1). In one study of patients undergoing reoperations for congenital heart failure, as many as 15% had already endured three previous operations during treatment. Furthermore, 15.1% of the entire group went on to experience severe morbidity, while 3.6% of patients died during the treatment period (Giamberti et al. 2009, 1286). The generation of postsurgical pericardial adhesions further contributes to the complications seen in follow-up procedures, prompting investigation to determine a reliable solution.

Pathogenesis of Adhesions

Pericardial adhesion formation after surgery can be best described as a type of healing response that occurs following damage to the heart tissue during the procedure. Previous investigations have shown that these processes begin quickly following surgical entry into the pericardium, as normal tissue morphology is disrupted in response to the incision. Pericardial mesothelial cells, or PMCs, which normally appear flat and in close contact within their native tissue layer, take on a rounded shape and eventually become dislodged after hours of surgery. During this time, an influx of blood and early inflammatory responses have also been observed as platelets and inflammatory cells are collected in the affected area. Additionally, due to the loss

of fibrinolytic action caused by a decrease in PMC number, fibrin deposits build up over time, providing a foundation for future adhesions (Cannata et al. 2013, 1819). In the days following surgery, fibrin deposition continues as fibroblasts and additional inflammatory cells collect on the surface of the pericardium. The fibrin structures themselves provide support for new connective tissue around the heart within the chest cavity following closure. Collagen is also produced in the region as a part of the growing extracellular matrix. Eventually, adhesions can become extremely dense around the immediate area, forming strong connections between the neighboring cardiac tissues. In some cases, the heart can become firmly attached to the sternum. Further growth can occur as the new adhesive tissue becomes vascularized over time, providing an additional source of bleeding during future surgical procedures (Cannata et al. 2013, 1820).

Many of the complications caused by postsurgical adhesive tissue during follow-up cardiovascular procedures are due to their nature as an obstacle for surgeons. Studies within animal models have previously shown that the presence of adhesions produces an impairment in heart function evidenced by decreased diastolic filling of the left ventricle (Cannata et al. 2013, 1). In human subjects, this has been accompanied by the impairment of normal heart function following surgery (Zhou et al. 2010, 1). Additionally, an increase in patient morbidity is seen during subsequent operations due to additional complications produced by adhesions (Ten Broek et al. 2016, 13). These include longer procedure times needed to carefully dissect this new tissue to access the heart, producing additional strain on the patient as well as those performing surgery. Visibility is also greatly reduced due to extensive tissue formation, creating difficulty in identifying the various structures within and around the heart which can be intensified due to bleeding by dissected vascularized adhesions. These factors can ultimately prevent access to the heart tissue and, in some cases, result in hemorrhaging of healthy tissue during reentry which

negatively affects the patient's safety (Konertz et al. 2003, 1270). Therefore, the development of a method for the prevention of postsurgical cardiac adhesions is vital to ensure the health and well-being of those involved during standard cardiovascular procedures.

Prevention of Adhesions

Several techniques for adhesion prevention have been proposed in recent years which stem from applications of biological principles as well as an implementation of chemical and physical barriers. The regeneration of PMCs within the affected area has been studied as a means of initiating natural regeneration within the patient after surgery (Cannata et al. 2013, 1820). This is based on the understanding that due to the fibrinolytic activity of this cell type, the construction of the initial fibrin scaffold can be prevented by recovery from PMC loss. A recombinant form of human keratinocyte growth factor (KGF), a known promoter of PMC proliferation, was previously tested for this purpose, and was shown to reduce the intensity of adhesions in subjects. However, it has been noted that the extent of fibrinolytic action by PMCs as well as the stability of the proliferating PMCs themselves is not well characterized and requires further study (Cannata et al. 2013, 1820). Additionally, the mechanism of PMC-based regeneration following trauma, including the effects of fibrinolysis, has also been a source of speculation among those in the field. Further studies have attempted to address the promotion of fibrinolysis directly using plasminogen activator and streptokinase with some success but have also been associated with unwanted bleeding and trauma in animal models (Cannata et al. 2013, 1820). An additional method of treatment based on the reduction of normal inflammatory response has also been investigated and has primarily focused on the use of specialized drug therapies. Agents such as dexamethasone, antibiotics, and NSAIDS have been applied through injection-based, oral, or targeted therapies and have demonstrated a significant decrease in

adhesions (Cannata et al. 2013, 1821). However, these therapies require clinical testing and have been reported to produce adverse effects related to an impaired healing response and internal bleeding (Cannata et al. 2013, 1823).

In addition to treatments based on biological mechanisms and drug-based therapies, the use of biomaterials has produced promising results in the reduction of adhesive pericardial tissue. This is best demonstrated by the implementation of "anti-adhesion barriers" that do not inhibit normal healing responses, but rather prevent adhesions simply by physical separation of distinct regions of tissue. For this reason, there is a consensus that an implanted barrier should not only degrade over time, but also have minimal interaction with internal wound healing (Cannata et al. 2013, 1822). Resorbable barriers made from extracellular matrix (ECM) components have been shown to reduce adhesion intensity scored by investigators and have even been able to facilitate proliferation of the patient's cells to the affected area for normal regeneration (Cannata et al. 2013, 1822–23). Additional polymeric barrier constructs made from chitosan have also shown promising results in animal models (Zhou et al. 2010, 803–4). These approaches, however, require further experimentation and clinical data. Additionally, the mechanism used by these materials to prevent adhesions is not well understood (Zhou et al. 2010, 803–4).

Several existing barriers for adhesions generated in various regions of the body are made from a variety of polymers and are currently available as commercial products. Seprafilm, designed specifically for this purpose, is made from a formulation of carboxymethylcellulose and hyaluronic acid to form a gel layer that hydrates and swells after implantation. While the material has technically been shown to reduce both the strength and the extent of pericardial adhesions formed, data taken from multiple studies has indicated that therapeutic effects are not significant, with only a 10% decrease in coverage reported in one case (Cannata et al. 2013, 1822–23).

Additionally, Seprafilm has been shown to demonstrate adverse effects such as inflammation in some areas of the body when applied (Diamond et al. 2012, 255). Similarly, REPEL-CV, a sheet formed with poly(ethylene glycol) (PEG) and poly(lactic acid) (PLA), has not been able to prevent adhesion formation within the chest cavity despite being proven to mitigate adhesion intensity. The surgical sealant Coseal, a PEG-based gel designed to act as a seal for sutures applied during surgery, has been demonstrated to reduce adhesion intensity by directly preventing the deposition of fibrin to the trauma site when applied. The barrier itself is also resorbed in 30 days following surgery, allowing coverage during a significant phase of wound healing (Cannata et al. 2013, 1820–22). However, it has also been noted that Coseal is subject to significant swelling and has been shown to cause surgical complications such as cardiac tamponade in some cases (Annabi et al. 2016, 4).

Based on the current state of available therapeutic options, it is important to design a novel anti-adhesion barrier that can be applied during standard cardiothoracic procedures. In order to prevent the formation and intensity of adhesions after surgery, the solution proposed must possess optimal mechanical and degradation properties within the chest cavity while maintaining high biocompatibility and low cytotoxicity. When evaluating the physical and chemical properties of the barrier, it is important that the material possesses sufficient elasticity in order to comply with the mechanical environment of the chest cavity while also attaching to the tissue to prevent premature material loss (Parlato, Matthew; Reichert, Sarah; Barney, Neal; Murphy 2014, 1). Adequate degradation time is also vital to ensure that the barrier is present during the weeks following surgery when adhesion growth is most prevalent. In addition, one should also consider whether the components used within the material are conducive to cell migration and regeneration in the treated area. PEG is a popular choice as a core component of

implantable hydrogels with tunable mechanical properties that can be adjusted by functionalization and crosslinking of the polymer. These modifications can also be used to adjust residence time in vivo. Additionally, PEG is also known to be both biocompatible and resistant to adhesion by native cells or tissue, making it a viable option as a potential solution (Parlato, Matthew; Reichert, Sarah; Barney, Neal; Murphy 2014, 1–2).

Dopamine-Modified Anti-Adhesion Barrier

The Christman lab has focused on the development of a novel hydrogel for the prevention of postsurgical cardiac adhesions in recent years. To this end, previous research has produced a chemical formulation that not only possesses favorable degradation characteristics in vivo, but also binds to the epicardium upon application in order serve as a reliable barrier for adhesion prevention. This has been achieved by the implementation of an 8-arm star PEG polymer modified with complimentary functional groups that are able to interact with one another as well as with the surface of the heart. Early data from experimentation with this new hydrogel has indicated favorable mechanical properties and attachment to porcine heart tissue ex vivo. Additionally, the material has been shown to significantly prevent the formation of adhesions when applied in live animal models with no apparent toxic response by the native tissue after treatment.

In order to incorporate a polymeric hydrogel barrier for in vivo applications, it is necessary to consider the chemistry of the polymer itself as well as the chemistry of added functional groups. For this reason, early work by the Christman lab has identified the use of oxime bonds as a method of crosslinking existing PEG polymers to ensure rapid gelation of the material. Oxime bonds are formed specifically by reaction between an aldehyde group and a hydroxylamine as part of a condensation “click” reaction (Grover, Braden, and Christman 2013,

2936). When both groups are present in an aqueous solution, reaction between these two groups is highly favored and occurs spontaneously. The resulting bond is considered hydrolytically stable and therefore resists reaction with solvent particles, in this case water (Grover, Braden, and Christman 2013, 2937). This also means that the material is resistant to early degradation within the body following implantation. Oxime-crosslinked hydrogels have also demonstrated satisfactory mechanical properties, low swelling, and do not promote proliferation by inflammatory cells in vitro (Grover, Braden, and Christman 2013, 2938). The gelation time of the material can be adjusted by both the environmental pH during oxime bond formation as well as the concentration of functionalized PEG components. In the formulation used in this study, PEG-AO and PEG-Ald polymers form linkages in PBS solution at 100 mg/mL each (Grover et al. 2015, 1329). The ratio of components used has been shown to play a vital role in the performance of the gel when used for therapeutic purposes. The virtually instantaneous formation time is critical to creating a barrier to adhesion formation, while slow gelation times run the risk of serving as substrates that promote cell growth and can negatively impact the residence time of the material. Furthermore, early research into this formulation has demonstrated that the 1:1 ratio of these components exhibit lasting retention to the cardiac tissue ex vivo as well as high cytocompatibility (Grover et al. 2015, 1330).

Continued study into the use of this oxime-crosslinked hydrogel has shown that material properties can be potentially enhanced by using the catechol group dopamine hydrochloride. The use of this chemical is inspired by its presence in mussels, which use dopamine to form adhesions in their wet native environments (Y. Liu et al. 2014, 16982). For this reason, dopamine has been incorporated into the design of numerous medical devices, especially implants, to ensure retention of the material in vivo. When oxidized spontaneously, catechol groups can

readily form linkages with amine and aminooxy groups through either Michael additions or Schiff base formation as demonstrated in Figure 1.1 below (Yang et al. 2016, 2).

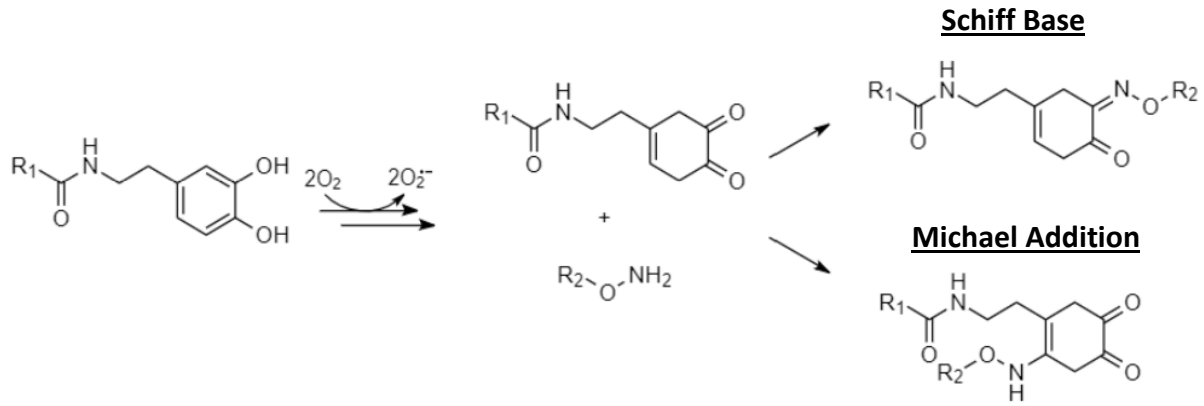

Figure 1.1: General process of the oxidation of the dopamine functional group followed by reaction with an aminooxy group to form Schiff bases and Michael additions. This process is necessary to increase the mechanical properties and further crosslinking of the Ald-AO-DOPA gel over time.

Dopamine oxidation not only allows further crosslinking with PEG-AO, but also with proteins present on the surface of human tissues, allowing greater retention of the gel in vivo. This can be achieved by functionalization of the same PEG polymers used in the synthesis of PEG-AO and PEG-Ald to form PEG-DOPA. This modification of the original gel structure has been associated with superior mechanical properties as well as high biocompatibility. This has previously been validated through experimentation in vivo using murine adhesion models, in which gels including PEG-DOPA were used to form a barrier over the surface of the heart abraded by repeated poking with needle tips after tearing of the pericardium. During this study, it was also shown that this new iteration of the material prevented adhesions to a greater extent than the original gel over a four-week period, with no inflammation observed (Fujita et al. 2018, submitted). Based on these results, the novel hydrogel barrier is currently being entered into testing within large animal porcine models.

For the proposed material to be effectively implemented as a working medical device, two additional points must be addressed in addition to the data obtained from animal models. First, the cytotoxicity of the gel must be evaluated in vitro as a means of indicating the biocompatibility of the material when implanted in animal models and, ultimately, human patients. The question of cytocompatibility with regards to the proposed Ald-AO-DOPA material arises primarily due to the inclusion of the catechol group in the gel formulation. Early trials within this project performed using elution products of the gel in media as well as polymer fractions incubated with cultured fibroblasts demonstrated that Ald-AO-DOPA and PEG-DOPA both caused significant cell death. This appears to conflict with histological data taken from the small animal in vivo studies, in which no necrotic response was detected (Fujita et al. 2018, submitted). However, research into biomaterials for applications such as regeneration and wound healing have also produced hydrogels that incorporate dopamine as a functional group to allow better adhesion to the tissue at the site of implantation (Y.-W. Liu et al. 2003, 16987). Therefore, determining the mechanism of this behavior, as well as a potential method of preventing cell death by the material, is important in order to implement this solution within a more relevant in vivo setting.

In addition to the issue of cytotoxicity, it is important to consider the method of material delivery to the surface of the heart tissue. When applying the material in the murine model, delivery was achieved using an existing air-driven applicator head that could accommodate two solutions in PBS, one with only PEG-AO and another with both PEG-Ald and PEG-DOPA, to form the gel. Despite achieving a 1:1 ratio of each, this method is best for small surfaces due to the dispersion of large droplets which may not distribute evenly over larger areas. Therefore, a new method of delivery must be considered in future experimentation and, ultimately, clinical

applications. This poses a challenge due to the equal mixing required for material formation as well as the rapid gelation time of the material, which lasts 2-3 seconds (Fujita et al. 2018, submitted). Many modes of delivery have been used for existing hydrogel products including surgical implantation, catheters, and even variations of air-driven sprays. In each of these cases, however, the above constraints must be satisfied to validate any particular technique. This can be accomplished computationally as well as through physical experimentation.

The development and implementation of a barrier for the prevention of postsurgical adhesions is an important step in solving a significant clinical issue. The benefits of the Ald-AO-DOPA material involved are clearly illustrated by preliminary studies given its effects on inhibiting the pathogenesis of adhesive tissue. By addressing the issues of in vitro compatibility and material delivery, the constraints imposed by the formulation of the gel can be resolved through experimentation. In this way, a novel solution can be applied to resolve a prominent medical issue.

Aims

Aim 1. Evaluate the biocompatibility of a dopamine-modified hydrogel (Chapter 1).

Previous studies using the Ald-AO-DOPA gel in murine cardiac abrasion models demonstrated significantly reduced intensity of pericardial adhesions after 4 weeks with no inflammation or necrotic response produced by the gel. However, dopamine, a known biological component, has been known to induce significant cell death when added on its own in vitro. Additionally, early biocompatibility studies of this hydrogel in vitro indicated a large reduction in cell viability during incubation. Due to the increased levels of dopamine used in this material relative to other existing materials, this study will be concerned with identifying the exact cause

of cell death produced by Ald-AO-DOPA gel. Additionally, to address potential discrepancies between the material's in vitro and in vivo behavior, further experimentation will provide a plausible solution to preserve cell viability in culture when the hydrogel and its components are applied based on the data obtained from metabolic and morphological assays.

Aim 2. Develop a method of delivery for a two-component oxime-bonded hydrogel (Chapter 2).

In order to successfully apply the hydrogel to the surface of the heart during clinical procedures as intended, it is important to use a technique that can apply the material evenly across larger surface areas. This study will be concerned with the development of a spray-based device that can be easily implemented and can accommodate the inherent kinetic properties of gel formation. This will be achieved by numerical simulation by computational fluid dynamics in order to predict the distribution of the two component solutions produced by air flow during spray, as well as by designing and ultimately testing a device based on the information gained through simulation studies in order to validate this technique as a feasible method of delivery.

Chapter 2:

Evaluation of the Biocompatibility of a Dopamine-modified Hydrogel

Introduction

The cytocompatibility of oxime-bonded hydrogels has been addressed in previous studies related to the prevention of cardiac adhesions, as evidenced by Grover et al. (1) during testing. However, early cell viability assays performed in vitro during the development of the Ald-AO-DOPA hydrogel by Fujita et al. using elution products of the hydrogel in cell culture media demonstrated significant cytotoxicity when components were added to cell culture with L929 murine fibroblasts. This result appears to conflict with in vivo animal studies using this material, where neither an inflammatory nor a necrotic response was produced four weeks after implantation in murine models (Fujita et al. 2018, submitted). At first glance, this also appears to conflict with other studies that have proposed implantable biomaterials utilizing dopamine with no reported cytotoxic response during biocompatibility testing in vitro, one of which was also formed from functionalized PEG (Liu et al. 2014, 16987). However, it should be noted that Ald-AO-DOPA gel studied here incorporates different concentrations of its component polymers compared to these materials (Liu et al. 2014, 16987). The 1:1:0.75 ratio used is vital to the mechanical properties and retention behavior of this hydrogel established by earlier experimentation. By contrast, existing materials functionalized with catechol groups tend to use a significantly lower concentration of dopamine, which may prevent a cytotoxic response observed at higher levels (Y. Liu et al. 2014, 16983). While polymers modified with dopamine are generally considered to be biocompatible, further analysis of a cytotoxic response due to higher dopamine functionalization in the proposed hydrogel may be required. Additionally, this study identifies a solution to dopamine-induced toxicity in vitro that also accounts for its favorable behavior demonstrated in vivo.

It should be noted that the detrimental effects of dopamine alone in vitro have been well established by previous studies. While it is known to play an important biological role in human systems, particularly in the brain, certain mechanisms occurring both independently and through enzyme activity have been shown to facilitate necrosis and apoptosis of multiple cell types in response to this catechol (Clement et al. 2002, 414,416). Given that dopamine plays a vital role in the formation of the proposed material over time, contributing to increased retention time and enhanced mechanical properties, it is critical to address whether this effect is observed when this catechol group is conjugated to a commercial PEG polymer within the larger hydrogel network. Therefore, this study will be primarily concerned with the detrimental effects of adding PEG-DOPA and Ald-AO-DOPA to cell culture as well as the specific cause of the reduced cell viability under these conditions.

Previous studies have associated the cause of cell death produced by free dopamine with its tendency to spontaneously oxidize under cell culture conditions, which produces both reactive derivatives of dopamine itself along with other reactive oxygen species (ROS) that serve as by-products of these reactions (Clement et al. 2002, 414). Much of the investigation into this subject has focused on Parkinson's disease, as dopamine accumulation and oxidation has been associated with resultant cell damage (Segura-Aguilar et al. 2014, 901). As a well-known hazard to living systems, ROS can adversely affect important cellular structures by reacting with fats, proteins and DNA (Y.-W. Liu et al. 2003, 287). As a catechol, free dopamine is known to readily generate several of these products beginning with a reaction with molecular oxygen through autoxidation. In earlier steps, this occurs by the reaction of oxygen with the pair of hydroxyl groups seen on the ringed portion of the dopamine structure. This results in the generation of two superoxide radicals, or O2.-, which react further to produce two moles of hydrogen peroxide, or

H2O2, per one mole of dopamine. This product can also react through a series of steps to form hydroxyl radicals, OH.,¬in the presence of iron, which greatly contributes to the state of oxidative stress on viable cells (Segura-Aguilar et al. 2014, 900–901). Due to its significance as an ROS in this process, H2O2 can serve as a quantifiable indicator of the state of oxidative stress within the cell culture environment in the presence of dopamine. Due to the fact that the crosslinking of the material is partially dependent on the formation of Schiff bases through the oxidation of dopamine functional groups, this presents a potential hazard in vitro when testing both the Ald-AO-DOPA gel and PEG-DOPA polymer with cultured cells (Yang et al. 2016, 2).

As a highly reactive species, OH. can disrupt the normal function of cells by acting on the molecules mentioned above. In the case of dopamine oxidation, both DNA base damage and lipid peroxidation have been identified as major effects of the resulting oxidative stress by multiple studies (Osiewacz, Hamann, and Zintel 2013, 965:283). Lipid peroxidation in particular has been noted as the most prominent indicator of oxidative stress. This process involves the oxidation of polyunsaturated fatty acids to form radical lipid species that can subsequently oxidize other molecular species or additional fatty acids as part of a chain reaction which creates further lipid radicals. Ultimately, this process terminates in the reaction of two different radicals or the creation of a reactive aldehyde group, which can cause death through multiple pathways. The chemistry and structure of these aldehyde groups can also cause the disruption and breakup of healthy cell membranes (Osiewacz, Hamann, and Zintel 2013, 965:284).

In addition to the formation of ROS species, it is important to consider the roles of dopamine derivatives in the generation of cytotoxic responses. During the oxidation process, reactive dopamine o-quinone and dopamine o-semiquinone are produced as a result of the initial reaction steps described above. These groups are further oxidized spontaneously to form

products such as aminochrome and 5,6-dihydroxyindole, which can result in additional H2O2 generation. Aminochrome is formed when further oxidation of dopamine o-quinone occurs, resulting in cyclization of the molecule through its amine group (Segura-Aguilar et al. 2014, 900). This occurs rapidly under physiological pH due to the instability of dopamine o-quinone under these conditions. An additional oxidation step can occur here by generation of 5,6-indolequinone from singlet O2. However, studies have indicated that this step may only occur in vitro, as the presence of certain enzymes in vivo promptly scavenge aminochrome by conjugation with the antioxidant glutathione (GSH) (Segura-Aguilar et al. 2014, 902). It should be noted that while the formation of aminochrome occurs relatively quickly, the rate of conversion to 5,6-indolequinone is noticeably smaller, causing a buildup of aminochrome in vitro. The general process of this oxidation is presented in the Figure 2.1 below, adapted from the scheme presented by Segura-Aguilar et al. (903).

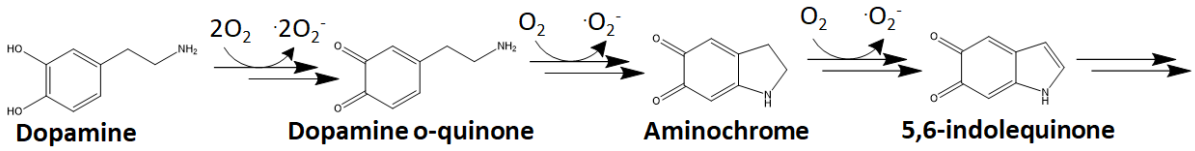

Figure 2.1: General mechanism of free dopamine oxidation. Note the production of multiple superoxide molecules, which react further to form hydrogen peroxide and hydroxyl radicals.

While the effects of ROS on cell apoptosis are well characterized, the mechanisms used by dopamine metabolites are still somewhat unclear. Dopamine o-quinone and 5,6-indolequinone have been noted for their relatively low stability, making them something of an unknown when attempting to determine a specific cause for cytotoxicity. Aminochrome, on the other hand, has been known to react with several proteins relevant to both in vivo and in vitro conditions. In neural tissue, this molecule conjugates readily with physiologically relevant proteins such as alpha synuclein and Parkin, both of which enhance neurotoxicity by inhibiting normal biological

processes in the progression of Parkinson's disease. Despite its relative instability, dopamine o-quinone has been known to affect cellular processes on a broader scale due to its ability to interact with mitochondrial electron chain complexes and other cellular components to form adducts that directly interfere with cellular metabolism. In this way, both dopamine o-quinone- and aminochrome-derived products can serve as potential markers for an alternative mechanism of dopamine-induced cell death (Segura-Aguilar et al. 2014, 903–4). Due to the fact that the dopamine used in the proposed hydrogel is favorably reacted with the functionalized PEG polymer through its amine group, cyclization should not spontaneously occur to create the products discussed here. However, it is possible that small amounts of unreacted dopamine that may still be present after purification. Therefore, determining whether the mechanisms described occur in vitro is important to establish the specific effects that the Ald-AO-DOPA hydrogel and its polymer components might have on living systems.

Previous attempts to address the cytotoxic response to dopamine in vitro have relied on the use of antioxidants in cell culture media. A variety of these molecules, which include multiple vitamins, enzymes and thiols, have been tested with multiple cell lines in order to isolate a reliable method of protection against oxidative stress and other damaging factors. Certain antioxidants, such as vitamin E, have been shown to be ineffective against cell death induced by dopamine. Ascorbic acid, a substitute of vitamin C, is an important biological component and commonly employed as a media supplement to ensure oxidative homeostasis (Choi et al. 2000). Certain studies have previously reported that this molecule can alleviate the effects of dopamine oxidation in cases when this process is not extensive and may therefore prove to be a viable option depending on the oxidative potential of the cell culture environment. Even when employing an effective antioxidant, however, the chemical nature of the dopamine

molecule itself should be taken into account. The enzyme catalase was used in one study and was tested with H2O2 and dopamine in both PC12 and M14 cell lines to determine its protective effects. While catalase prevented cell death in the former case, dopamine test groups showed only minor improvement (Clement et al. 2002, 417).

Glutathione has been widely studied as an established solution to the presence of excess dopamine and its products. As a member of the thiol family, GSH is ubiquitous in the body despite having a low plasma concentration (Michelet et al. 1995, 1509). GSH can fight traditional oxidative stress by reduction of H2O2 catalyzed by glutathione peroxidase found in culture serum, being converted to glutathione disulfide (GSSG) in the process. It is important to note that this molecule must be reduced enzymatically in order to regenerate GSH (Halliwell 2003, 5). Culture groups undergoing oxidative stress and dopamine treatment have both been shown to have depleted GSH intracellular levels, effectively removing antioxidant defenses and creating a need for an additional supply of GSH (Spina and Cohen 1989, 1398). Previous work has demonstrated that adding GSH to cell cultures treated with free dopamine successfully enhanced cell viability under these conditions, preventing cell death almost entirely (Clement et al. 2002, 419). As previously noted, glutathione is known to conjugate either enzymatically or spontaneously with dopamine o-quinone and aminochrome to form less toxic products (Segura-Aguilar et al. 2014, 902). By examining the effects of multiple biologically relevant antioxidants on dopamine in vitro, a better understanding of this functional group's oxidative behavior in vivo can be achieved.

Methods

Synthesis of 8-arm PEG-NPC

10 g of 8-arm PEG (10k) was dried under vacuum for 3 hours, with stirring, at 60°C. Melted PEG was then cooled to 30 °C and dissolved in 200 mL anhydrous dichloromethane (DCM) under argon. Once completely dissolved, 16.96 g 4-nitrophenylchloroformate (NPC), 24 mL trimethylamine (TEA), and 1.028 g dimethylaminopyrrolidine were added to the solution and allowed to react with stirring for 3 hours. This was performed in an ice bath due to the exothermic nature of the reaction. Product was precipitated by adding 1L of anhydrous ethyl ether in a 2L beaker with stirring before being filtered by vacuum. The precipitate was then allowed to dry overnight under vacuum. H1 NMR analysis displayed multiplets at 8.26 ppm, 7.38 ppm 4.43 ppm and 3.85-3.35 ppm.

Synthesis of 8-arm PEG-DOPA

PEG-NPC was added to a round bottom flask with stirring at 60 °C and dried for 3 hours. Additional reactants and reagents were added in defined molar ratios to functionalized PEG. Under argon, anhydrous 1-methyl-2-pyrrolidone (NMP) was added (20:1) along with TEA (80:1) and dopamine hydrochloride (80:1). The reaction was allowed to proceed with a condenser under argon for 12 hours. The solution product was then transferred to dialysis tubing and placed in 1M acetic acid buffer. Dialysis was allowed to proceed for 48 hours, with the buffer being replaced every 24 hours and discarded. The product was then dialyzed against 0.5 M acetic acid buffer for an additional 48 hours. Finally, the product dialyzed against methanol for 72 hours under the same conditions before being vacuum filtered and isolated via rotary evaporation. H1 NMR

analysis yielded multiplets at 7.20 ppm, 6.59 ppm, 6.53 ppm, 6.39 ppm, 4.03 ppm, 3.85-3.35 ppm, 3.40-3.05 ppm. Products were stored in a desiccator until further use.

Synthesis of 8-arm PEG-Ald

Star 8-arm PEG polymer (10k) was dried under vacuum at 60 °C for 3 hours with stirring. Under argon, at 30 °C, 200 mL DCM was added to dissolve the dried polymer before adding 3.603 g 4-carboxybenzaldehyde. The reaction was moved to an ice bath and 4.601 g N-(3-Dimethylaminopropyl)-N'ethylcarbodiimide hydrochloride (EDAC) was added. The reaction was allowed to proceed for 48 hours. Methanol (50 mL) was added to the reaction which was allowed to proceed for 3 additional hours. The product was placed on dialysis against methanol for 3 days, with methanol being exchanged and discarded each day. NMR analysis produced a singlet at 10.08 ppm and multiplets at 8.19 ppm, 7.93 ppm, 4.49 ppm, and 3.85-3.35 ppm. The dialysis product was then dried under rotary evaporation and stored in a desiccator until use.

Synthesis of 8-arm PEG-AO

PEG (10.10 g) was dried under vacuum as previously described. The dried polymer was dissolved in 90 mL DCM before adding 10 mL tetrahydrofuran (THF), 9.23 g N-hydroxyphthalimide, and 14.84 g triphenylphosphine before placing in an ice bath. Diisopropyl azodicarboxylate (11.14 mL) was then added dropwise for 30 min before allowing the reaction to proceed for 72 hours. Methanol (7.5 mL) was then added before allowing the reaction to proceed for another 3 hours. The product was dialyzed against methanol for 72 hours and subsequently dried via rotary evaporation to yield PEG-hydroxyphthalimide (PEG-HPT), which was then dried on vacuum overnight. PEG-HPT was dissolved in 300 mL acetonitrile as 6.77 mL hydrazine monohydrate was added dropwise over 15 minutes. The reaction was allowed to

proceed for 48 hours before isolating the crude product by vacuum filtration and drying with rotary evaporation at 30 °C. NMR analysis displayed multiplets at 3.88-3.85 ppm, 3.8-3.4 ppm. These steps were repeated once before allowing the product to dry on vacuum overnight.

Peroxide Assay

An assay to measure the concentration of H_2O_2 in cell culture media was performed utilizing the Pierce Quantitative Peroxide Assay Kit for aqueous solutions (Thermo-Fisher Scientific). This test was performed on media taken from the sample groups containing both the hydrogels and polymers in cell culture as well as an identical media incubated for 24 hours containing the same materials without the presence of cells. A standard curve was prepared utilizing a 30% H_2O_2 stock solution (9.8 M) diluted with DMEM (high glucose, 10% FBS, 0.5% P/S) to achieve a concentration of 1 mM. Six subsequent dilutions were performed by adding 100 µL of DMEM to 100 µL of the preceding H_2O_2 solution, resulting in solutions with a peroxide concentration half that of the previous solution. A volume of 20 µL of each solution was added to corresponding wells of a 96-well plate, before being treated with 200 µL of prepared reagent solution. The reagent itself was made by adding Reagent A provided by the assay kit (2.5 M H_2SO_4, 25 mM ammonium ferrous (II) sulfate) to Reagent B (aqueous solution of 100 mM sorbitol, 125 µM xylenol orange) in a 1:100 ratio. The solutions were then allowed to incubate for 15 minutes at room temperature. The low pH achieved by addition of H_2SO_4 favors oxidation of iron from Fe^{2+} to Fe^{3+}, which then forms a complex with xylenol orange to produce a color change that can be quantified by absorbance readings. Absorbance itself was measured via plate reader at a wavelength of 595 nm, and the readings obtained were plotted against known H_2O_2 concentrations to produce a standard curve.

Media samples were prepared in a manner similar to that of the test groups used during elution assay experiments. Briefly, 10k/10k/Cat gels were prepared in 1.5 mL Eppendorf tubes to yield 34 µL of gel before adding 0.5 mL of media. Solutions of the polymer components in media were prepared using 5.10 mg/ mL PEG-DOPA and 6.80 mg/mL each of PEG-Ald and PEG-AO. Additionally, test groups including equivalent concentrations of antioxidants performed in cell culture, both GSH (5.22 mg/mL) and ascorbic acid (3.0 mg/mL), were prepared in test groups containing either PEG-DOPA or Ald-AO-DOPA. Each of these groups was incubated for 24 hours at 37 °C and 5% CO2. Equal amounts and concentrations of gels and polymers were added to cell culture samples. Samples were then prepared in a 96-well plate using 20 µL of each test group along with 200 µL of the accompanying reagent solution. Additionally, blanks were prepared using 20 µL of media together with the reagent solution. All groups were then incubated at room temperature for 15 minutes before being measured for absorbance at 595 nm and plotted to determine peroxide concentration with or without cultured cells according to the calculated standard curve.

Fluorescence Microscopy

An ImageIT Lipid Peroxidation Kit was used to assess the extent of oxidation effects on cellular lipids. L929 cells were cultured as previously described before seeding five separate groups (n=3) in 24-well flat-bottom plates at a density of 9.50×105 cells/well in DMEM (10% FBS, 0.5% P/S). Cells were then incubated for 24 hours at 37°C, 5% CO2. Culture media was aspirated, and test groups were prepared by using samples treated with 5.10 mg/mL PEG-DOPA in fresh DMEM (0.5 mL). Additionally, PBS (1:10, v/v) in media was used as a negative control, while 1mM H2O2 in media was used as a positive control. Two more test groups were prepared by adding 5.22 mg/mL GSH and 3.00 mg/mL ascorbic acid to culture containing 5.10 mg/mL

PEG-DOPA. The plate was then incubated for 24 hours at 37°C and 5% CO2. The stock reagent of C11-BODIPY581/591 was then added to the media of all groups (1:1000, v/v) to obtain a concentration of 10 µM, which was then incubated under the same conditions for 30 minutes in darkness. The media was then aspirated before rinsing each cell layer in PBS. Fluorescence was then measured via a fluorescence microscope using DsRed and GFP filters for analysis of both red and green signals produced by normal and oxidized lipids, respectively. Excitation and emission for unaffected and oxidized lipids occurs at 581/591 and 488/510. The results obtained were then compared as a ratio of the measured fluorescence between the two lipid states to determine the extent of peroxidation in living cells.

NMR Spectroscopy

Samples were prepared in 15 mL Falcon tubes by adding 0.5 mL D2O to 34 µL Ald-AO-DOPA in one while adding 5.1 mg/mL PEG-DOPA in D2O to another. Both samples were incubated for 24 hours at 37 °C at 5% CO2. The PEG-DOPA solution and the elution product of the Ald-AO-DOPA gel were measured with one-dimensional H1-NMR spectroscopy using a Jeol eca500 machine. Spectra were collected and analyzed for peaks representing the dopamine products aminochrome and 5, 6-indolequinone.

Cell Culture

L929 murine fibroblasts were cultured with high-glucose DMEM supplemented with 10% fetal bovine serum (FBS) and 0.5% penicillin-streptomycin (P/S). Cells were allowed to grow to 70-90% confluency before plating. Cells were washed twice in 5 mL PBS and treated with 5 mL of 0.25% trypsin-EDTA and incubated for 7 minutes. The trypsin was then neutralized with an equal volume of culture medium, and the resulting cell suspension was

centrifuged at 1500 rpm for 5 minutes. The supernatant was then aspirated while the cell pellet was suspended again in 5 mL of culture media. Cell seeding was performed at a concentration of 190,000 cells/mL in 0.5 mL of media to each well in a flat-bottom 24-well plate to yield 95,000 cells per well. Plates were then swirled gently to ensure even distribution of cells and incubated at 37 °C and 5% CO2 for 24 hours, or until confluent.

Biocompatibility Assay

Following culture and seeding, fibroblasts were incubated for 24 hours at 37 °C and 5% CO2. At this point, micrographs were taken of a baseline sample of grown cells, which were then subjected to a metabolic assay by adding fresh serum-free media with alamarBlue reagent (1:10, v/v) and read for fluorescence intensity (550 nm excitation, 585 nm emission) after 2 hours. Test groups (n=3) were prepared from all component polymers and hydrogel formulations using concentrations and volumes equivalent to those used in peroxide assay studies. All polymer solutions were sterilized using 0.22 µL filters. Additionally, solutions in PBS were prepared using the antioxidants glutathione (5.22 mg/mL) and an equimolar amount of ascorbic acid (3.00 mg/mL) which were each applied to additional test groups of PEG-DOPA and Ald-AO-DOPA. Antioxidant solutions were added to the media 1:10 (v/v) in each new group. Positive and negative controls were prepared using PBS (1:10, v/v) and ZDEC (100 mg/mL) in fresh culture media. All test groups were incubated for an additional 24 hours at 37 °C with 5% CO2. Micrographs of both test and control groups were taken, and all groups were treated with premade alamarBlue solution and measured for fluorescence intensity after 2 hours of incubation at 37 °C.

Morphological Assay

Morphological analysis of cells was performed after incubation with gel products and polymer components with or without supplements. For experiments studying direct contact, micrographs were taken in triplicate from each of the three wells for each test group (n=9) along with positive and negative control groups and blinded before being scored semi-quantitatively based on the appearance of the cell. The scoring system used here is based on the criteria outlined by the International Organization for Standardization (ISO) in the official guidelines for establishing biocompatibility of a medical device in vitro as shown in the table below (ISO 15686-5 2008, 8). Images of the baseline group were not blinded, but instead used by graders as a reference to determine the extent or inhibition of cell growth.

Table 2.1: Grading criteria for cell morphology scoring of L929 fibroblasts, as outlined by ISO 10993-5.

Table 2.1: Cell Morphology Assay Criteria	
0	No cells rounded; no growth inhibition
1	< 20% of cells rounded; slight growth inhibition
2	< 50% of cells rounded; 50% growth inhibition
3	< 70% of cells rounded; greater than 50% inhibition
4	Complete cell destruction

Statistical Analysis

Analysis of results from the experiments described with three or more samples was performed using one-way analysis of variance (ANOVA) and post hoc Tukey's test. Significance was set to $p < 0.05$. Results with only two samples were compared using an unpaired t-test.

Results

Peroxide Assay

Measurement of the peroxide concentration was performed to determine whether ROS species were generated by the Ald-AO-DOPA gel. The results of the peroxide assay indicate that elevated levels of H2O2 are present after incubation of both PEG-DOPA and Ald-AO-DOPA with or without cells in culture media. The specific peroxide concentrations produced by the polymer component and the hydrogel were 0.337 ± 0.0174 mM and 0.369 ± 0.0197 mM in cell culture, and 0.304 ± 0.00579 mM and 0.305 ± 0.0129 mM in media alone. Samples with GSH had significantly lower concentrations of peroxides present in solution. The H_2O_2 concentration of test groups treated with ascorbic acid, while slightly elevated above untreated groups, significantly prevented the generation of peroxides in both environments. For samples in culture and in media alone, this reached only 0.0367 ± 0.00323 and 0.0383 ± 0.00912 for PEG-DOPA groups and 0.0391 ± 0.00324 and 0.0326 ± 0.00276 for Ald-AO-DOPA groups, respectively. Results are presented in Graph 2.1 below.

*Graph 2.1: Peroxide assay results from incubated media of polymer components and hydrogels with or without cultured L929 fibroblasts (***p < 0.0001).*

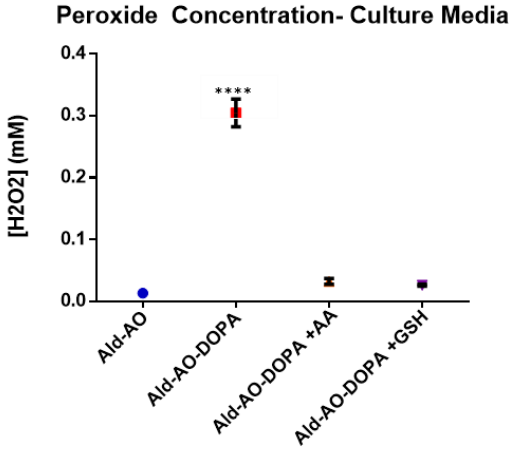

Fluorescence Microscopy

The fluorescent signals produced by the C11-BODIPY$^{581/591}$ marker measured through DsRed and GFP channels indicates a notable shift towards the green emission state in samples treated with PEG-DOPA relative to the negative control, as presented in Graph 2.2. The ratio of reduced to oxidized lipids in this group was found to be 5.01 ± 1.87 and was statistically different from the PBS-treated samples. While appearing slightly higher than fibroblasts treated with 1 M H_2O_2, no significance was reported between these samples compared to those treated with PEG-DOPA alone. Micrographs of each group are presented in Figure 2.2.

Addition of ascorbic acid or glutathione to samples treated with Ald-AO-DOPA or PEG-DOPA demonstrate significantly different ratios of fluorescence as seen in Graph 1.3. Fibroblasts exposed to PEG-DOPA in the presence of GSH maintain a high DsRed to GFP signal ratio, which appears significantly greater than the group supplemented with ascorbic acid. The ratios calculated from each group are 595 ± 468 and 3.65 ± 1.63 for GSH and ascorbic acid treatment.

*Graph 2.2: Results of fluorescence microscopy analysis via ImageJ for PBS, H_2O_2 and PEG-DOPA samples incubated with cells (**p = 0.0002).*

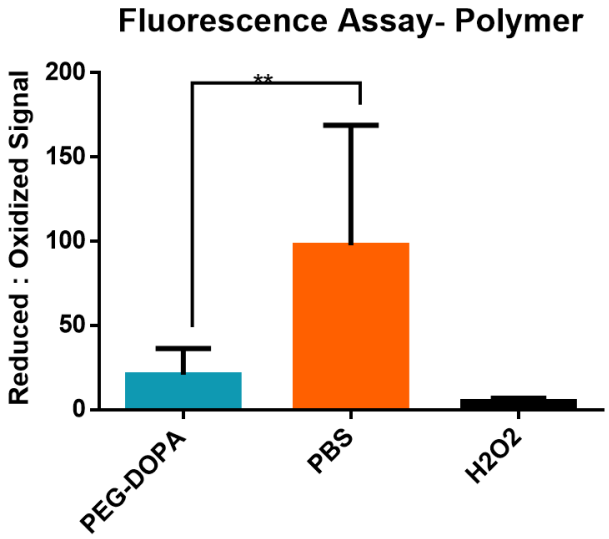

*Graph 2.3: Results of fluorescence microscopy analysis via ImageJ for cells incubated with PEG-DOPA and either ascorbic acid or GSH (**p = 0.005).*

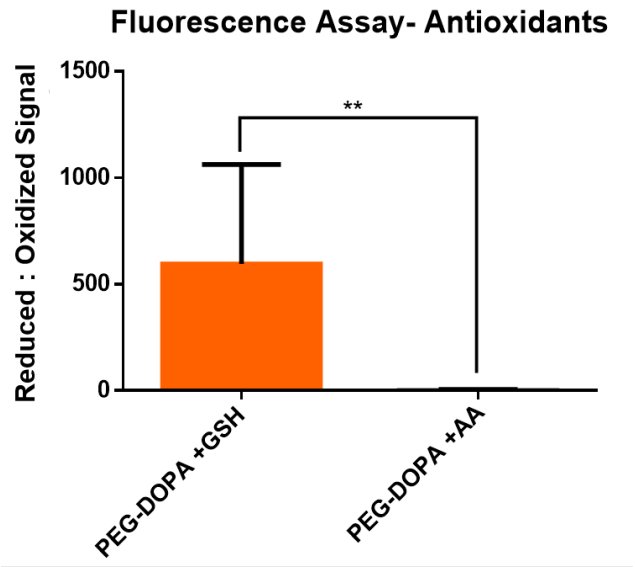

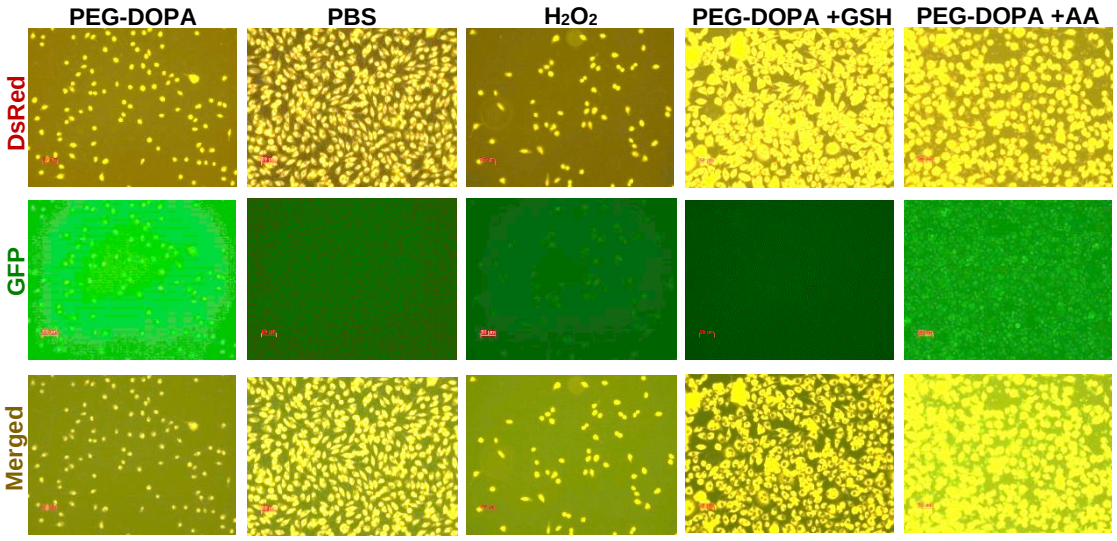

Figure 2.2: Fluorescence images taken from cultured cells using DsRed and GFP filters.

NMR Spectroscopy

NMR analysis was used to verify that no dopamine-specific oxidation products, which could contribute to cellular disfunction, were produced by the material. The spectrum produced

by the elution product of the Ald-AO-DOPA gel did not indicate the presence of free dopamine or any of its derivatives produced during oxidation. The peak at 4.67 ppm is produced by D_2O. Inspection of the spectrum (Figure 2.3) showed a notable peak at 3.56 ppm. Similarly, the equimolar solution of PEG-DOPA did not produce either aminochrome or 5,6-dihydroxyindole after 24 hours, as indicated in the figure below. This spectrum also contained a peak at 3.55 ppm as indicated in Figure 2.4.

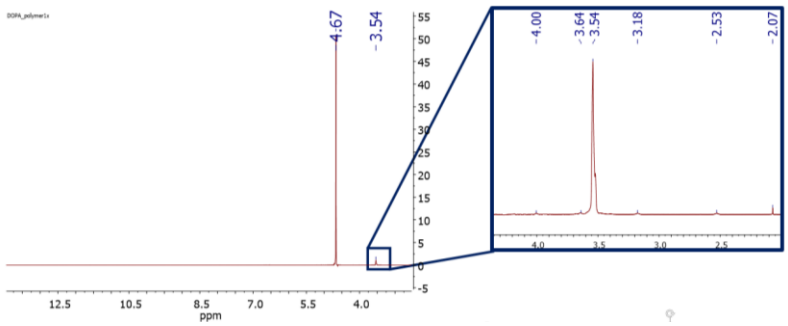

Figure 2.3: NMR spectrum produced by 5.1 mg/mL of PEG-DOPA incubated in D_2O for 24 hours. The magnified section at the right shows a small peak at 3.54 ppm along with other smaller peaks.

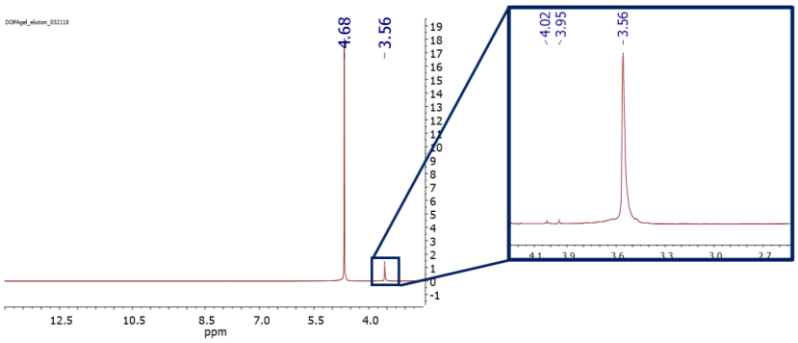

Figure 2.4: NMR spectrum produced by incubated Ald-AO-DOPA in D_2O. The magnified region at the right shows the presence of a peak at 3.56 ppm.

Biocompatibility and Morphological Assays

The alamarBlue assay indicated the viability of cells incubated with materials and polymer components through measurement of metabolic activity. Fluorescence readings revealed that cell viability was significantly decreased in test groups treated with PEG-DOPA and Ald-

DOPA alone, with fluorescence measurements of each group being less than 20% of those seen in groups treated with PBS. Neither PEG-Ald nor PEG-AO produced any significant change in signal. Addition of ascorbic acid to samples containing PEG-DOPA and Ald-AO-DOPA resulted in RFU readings of $1.70\times10^3 \pm 105$ and $2.24\times10^3 \pm 488$, respectively. Both PEG-DOPA and Ald-AO-DOPA groups treated with GSH (5.22 mg/mL) demonstrated significantly higher readings of $9.99\times10^3 \pm 1.02\times10^3$ and $8.59\times10^3 \pm 178$, respectively.

*Graph 2.4: Metabolic (alamarBlue) assay results after incubation. Data are reported as mean ± SD (****p < 0.0001).*

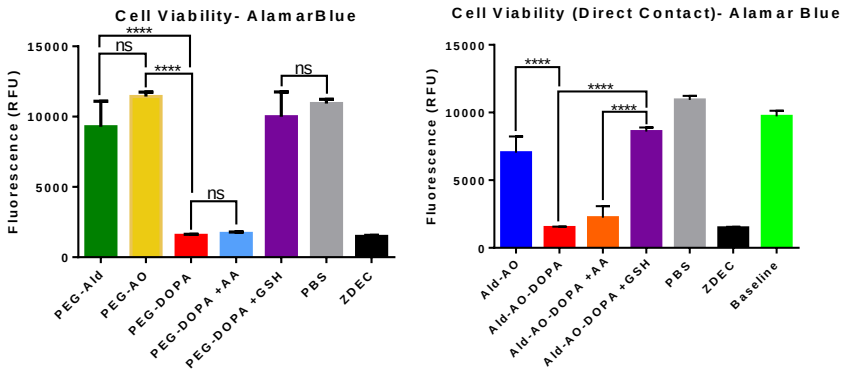

Morphological evaluation of these same groups (n = 9) produced average scores of 3.44 ± 0.176 and 3.00 ± 0.00 for PEG-DOPA and Ald-AO-DOPA, respectively, according to ISO-10993-5 standards. These groups also demonstrate an almost exclusively rounded morphology as pictured in contrast to the elongated shape of other test groups. No significant difference in these results was observed in groups additionally supplemented with ascorbic acid. Samples containing PEG-DOPA with GSH added earned an average score of 1.11 ± 0.111, while groups with Ald-AO-DOPA hydrogel had a score of 1.22 ± 0.147.

*Graph 2.5: Morphological assay results after incubation. Data are reported as mean ± SD (****p < 0.0001).*

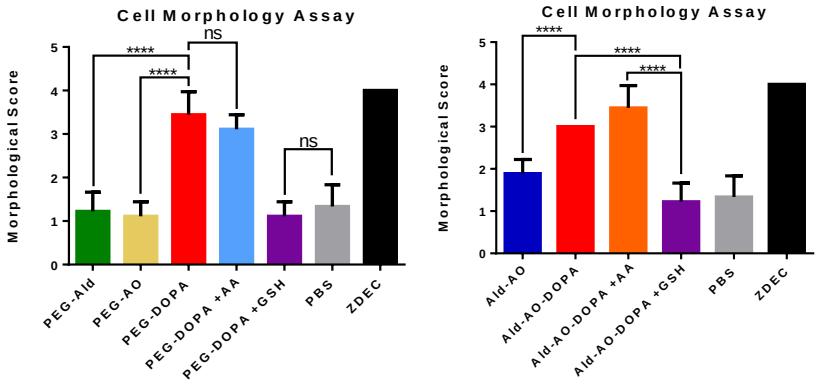

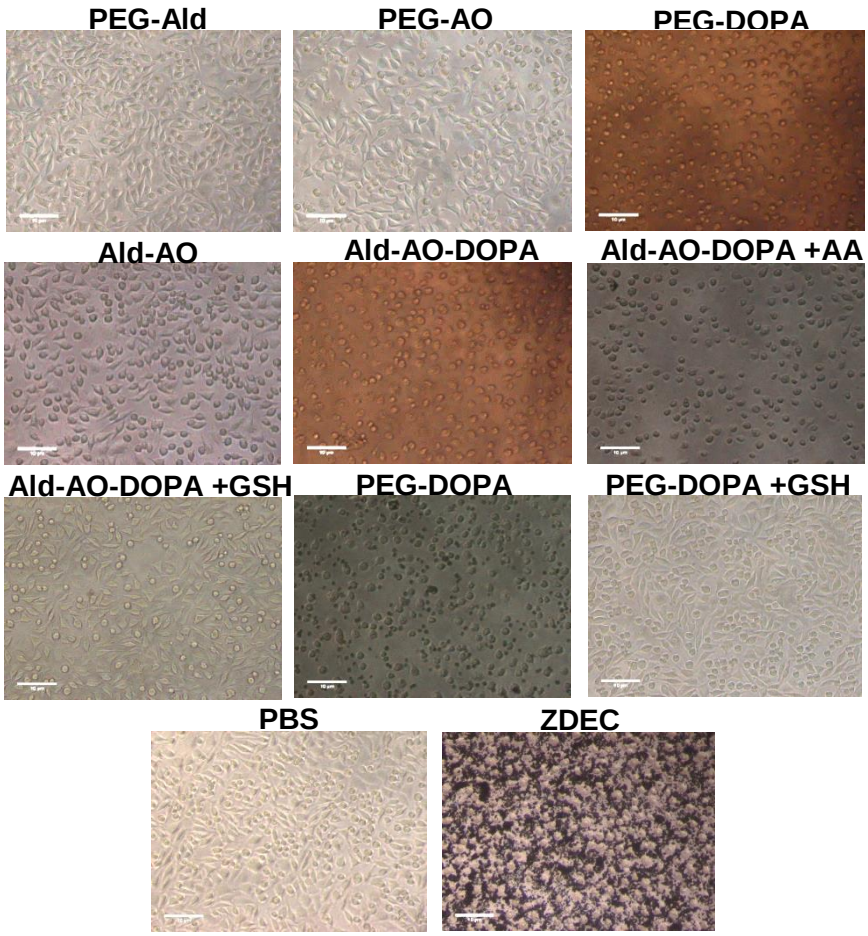

Figure 2.5: Micrographs taken of cell cultures from samples incubated with hydrogels or polymer components with or without antioxidant supplements.

Discussion

In addition to the fact that previous *in vivo* studies with this same type of chemically modified material have shown that no comparable response is developed after implantation, other hydrogel-based biomaterials functionalized with dopamine have also been developed with no adverse effects reported during *in vitro* studies (Liu et al. 2014, 16897). Based on the results of this study, however, it is apparent that the higher concentration of dopamine functional groups present in polymers used severely promotes cell death in culture due to the elevation of spontaneously generated products. Therefore, the inherent chemistry of the Ald-AO-DOPA necessary for enhanced retention presents an additional challenge to normal cell culture assays.

Absorbance readings obtained from the peroxide assay indicate the formation of H_2O_2 in cells through a color change caused by the reaction of xylenol orange dye with oxidized iron (Pierce 2012, 1). This trial confirmed that the addition of either Ald-AO-DOPA gel or PEG-DOPA to cell culture media generates significant levels of H_2O_2. This is a logical result based on known oxidation pathways of dopamine as well as the established crosslinking kinetics of the material, which require these spontaneous redox reactions involving dopamine for additional linkage formation by way of Michael additions and Schiff bases (Yang et al. 2016, 2). The concentrations of H_2O_2 were calculated based on absorbance readings taken from media samples incubated with and without live cell culture in order to determine the significance of normal cell growth on H_2O_2 production by dopamine functional groups. In all cases, peroxide concentrations fell within the range of 0.30 mM - 0.40 mM, with cell culture samples appearing to reach moderately higher levels. These levels are sufficient to induce adverse effects in cells during incubation (Whittemore et al. 1995, 923–24). However, within both cell culture and pure media samples, H_2O_2 levels were not significantly different between PEG-DOPA and Ald-AO-DOPA

groups, indicating that the formation of the complete gel compared to the presence of free polymer components in solution, has no effect on H_2O_2 concentration.

The results of NMR spectroscopy indicate that no additional oxidation products of dopamine other than those determined by the peroxide assay are generated during incubation for 24 hours. D_2O was used here in place of culture media since the oxidation process occurs spontaneously through oxygen exposure. In this analysis, aminochrome and 5,6-indolequinone were chosen due to the fact that they are the most stable products of reacted dopamine after extended periods (Segura-Aguilar et al. 2014, 900–903). However, NMR analysis performed in earlier studies using D_2O in H^1 NMR readings demonstrates the presence of multiple characteristic peaks that form across the spectra representing these derivatives, none of which are apparent in the measurements taken here (Bisaglia, Mammi, and Bubacco 2007, 15600). The small peak in each spectrum between 3 and 4 ppm is produced by the backbone of PEG, and is likely due to a slight release of unreacted polymer from the gel network from any of the three material components (Dust, Fang, and Harris 1990, 3745). Therefore, while the oxidation of the dopamine functional groups produces significant oxidative stress on the cellular environment, the generation of dopamine-based byproducts does not occur under these conditions. By extension, this also indicates that the dysfunction of cellular components caused by the formation of complexes between dopamine derivatives and organelle proteins is an unlikely cause of cell death.

To determine the significance of ROS to the viability of *in vitro* cultures, it is necessary to find a reliable method to detect the products of lipid peroxidation in cellular structures. Certain methods such as the TBARS assay, which uses thiobarbituric acid to measure aldehyde products of oxidized lipids, have been known to demonstrate low sensitivity despite allowing the detection

of specific products (Domínguez-Rebolledo et al. 2010, 360). As an alternative, fluorescence labelling is capable of lipid peroxide detection in environments with high oxidative stress. C11-BODIPY$^{581/591}$ acts as a label to track the state of oxidation within the culture environment by acting as an equivalent to fatty acids such as those found in cell membranes. While initially emitting significant fluorescence in the red region of the spectrum, oxidation of the probe produces a shift to emission in the green region. In this way, a ratio can be obtained to determine the prevalence of lipid peroxidation compared to the healthy cell condition (Image-it 2012, 1–2). This method can also be used to determine the protective effects of antioxidants added to culture as supplements.

The results of the fluorescence intensity readings obtained from C11-BODIPY$^{581/591}$ indicate that lipid peroxidation occurs in cells treated with PEG-DOPA. Additionally, samples incubated with PEG-DOPA together with ascorbic acid also indicated significant lipid peroxidation based on the decreased ratio of reduced to oxidized polyunsaturated fatty acids. This data, together with findings obtained from metabolic and morphological assays, shows that the elevated levels of H_2O_2 produced by this polymer induce oxidative stress on the cell environment. In addition, it is also shown that ascorbic acid fails to inhibit the effects of cell death through oxidative stress by PEG-DOPA. The opposite is true for the inclusion of GSH with PEG-DOPA, as lipid peroxidation is not apparent due to a higher reduced-to-oxidized ratio, demonstrating the ability of glutathione alone to prevent oxidative stress.

Fluorescence (RFU) signals obtained from alamarBlue readings in the biocompatibility assay indicate that significant cell death results from the inclusion of PEG-DOPA or Ald-AO-DOPA alone in culture. This outcome bears strong similarities to previous studies measuring the effects of dopamine molecules added to neuronal cells *in vitro*, indicating that the detrimental

effects of excess dopamine are still observed when the catechol is functionalized to polymer units. From this data, it can also be concluded that the cytotoxic effects of the Ald-AO-DOPA gel are due to the presence of PEG-DOPA alone, since neither PEG-AO nor PEG-Ald added to the media elicit a cytotoxic response. This assay also demonstrates that GSH is a suitable defense against the adverse effects of dopamine-based materials, as alamarBlue readings indicate that the viability of cells in these test groups is comparable to the values taken from the PBS control. The calculated average of the RFU readings from the GSH-treated samples of Ald-AO-DOPA and PEG-DOPA are 78% and 91% of that seen in the negative control. These readings are well above the minimum 70% viability established by ISO-10993-5 (18) guidelines, indicating adequate cell viability.

Treatment of fibroblasts with individual polymer components in media demonstrates that the production of ROS in culture is similar to the behavior seen in media alone. This shows again that H_2O_2 generation is exclusive to the inclusion of the PEG-DOPA component, as both PEG-Ald and PEG-AO caused no measurable increase in H_2O_2. Similarly, the Ald-AO hydrogel does not generate peroxide formation over time compared to Ald-AO-DOPA under the same conditions. In test groups both with and without cells, both ascorbic acid and GSH greatly reduced ROS concentrations. While PEG-DOPA and Ald-AO-DOPA samples treated with ascorbic acid yielded slightly higher concentrations, this effect was not significant, indicating that antioxidant is sufficient to prevent the formation of H_2O_2.

Interestingly, fluorescence readings for the Ald-AO-DOPA and PEG-DOPA groups treated with ascorbic acid showed that cell viability is not maintained when this antioxidant is used, as the increase in observed cell viability relative to non-supplemented counterparts was insignificant based on alamarBlue treatment, despite being able to reduce the levels of H_2O_2 in

media. Earlier studies have noted the relationship between dopamine and ascorbic acid, showing that the antioxidant can moderately improve cell viability under conditions where both are included in culture. However, in environments with higher oxidative potential, ascorbic acid can act as a cytotoxic agent. This is credited to the generation of ascorbyl radicals, which are part of a different family of ROS that can damage living cells which would not be detected by the peroxide assay used here (Choi et al. 2000, 82–83). This would explain not only the degree of cell death in samples with dopamine functional groups, but also the extensive lipid peroxidation shown by fluorescence studies.

The inclusion of a biologically relevant antioxidant, such as GSH or ascorbic acid, which can mitigate the detrimental effects of dopamine requires additional consideration due to the static nature of the cell culture environment. Due to the fact that the transport of bodily fluids, such as blood flow, is constantly at play within the tissue during the residence of the material, it is appropriate to add a concentration of this supplement that more closely reflects the total molar amount supplied to the heart over an extended period. For this reason, the concentration of glutathione used here is actually an order of magnitude higher than that found in whole blood in order to compensate for the stagnant media volume used in culture (Michelet et al. 1995, 1509). Within a 24 hour period in the human heart, assuming a total cross-sectional area of 2000 cm^2 for both capillaries and venules and an average velocity of 0.05 cm/s, as well as a whole-blood GSH concentration of 8.49×10^{-7} mol/cm^3, the amount of each antioxidant delivered to this region of tissue daily is well above the level used here (Jacob, Chappell, and Becker 2016, 6; Michelet et al. 1995, 1509). In this way, the experimental design used in this study better approximates the environment exposed to generated free radicals *in vivo*.

While alamarBlue is useful for measuring the metabolic activities of viable cells, morphological assay data was obtained to corroborate the findings of this original test. The data obtained from scoring appear to validate the results of the metabolic assay. Sample groups containing PEG-DOPA and Ald-AO-DOPA, as well as replicate groups containing ascorbic acid, demonstrated significantly reduced cell viability as the majority of fibroblasts had a rounded shape in each case. Each of these groups had an average score of at least 3. By contrast, the majority of cells in all other test groups, possessing an average score of below 2, had an extended and spindle-like shape. ISO criteria for *in vitro* morphology assays state that a score of above 2 in the range from 0 to 4 is indicative of a cytotoxic response by the species present, further showing that Ald-AO-DOPA or PEG-DOPA alone or with added ascorbic acid is detrimental to cell culture (ISO 15686-5 2008, 9). GSH, however, visibly maintains cell viability with no apparent effect on cell morphology relative to the negative control or baseline.

Chapter 3:

Development of a Method of Delivery for a Two-Component Oxime-Bonded Hydrogel

Introduction

In order to successfully implement the Ald-AO-DOPA hydrogel during treatment, an appropriate method of delivery is needed. Due to the inherent properties of the combined polymer components, the application of a complete hydrogel directly to the cardiac tissue requires a specific technique that considers the constraints imposed both by the material and the environmental conditions present during routine cardiac procedures. These include the rapid gelation time of the material, the stability of the oxime bonds against hydrolysis upon formation, and the limited available space within the open chest cavity (Grover et al. 2015, 1327). With this in mind, an ideal method of delivery would be able to operate at a distance of over 10 cm from the patient to ensure maneuverability by the user, which is generally recommended for current products (Chaurasia et al. 2012, 3). The device would simultaneously inhibit contact between the two component solutions in order to prevent premature gel formation while also creating a uniform layer on the tissue surface. To fulfill each of these requirements, the focus of this study is to design a novel device that can be validated through computational modeling together with testing of a working prototype.

The delivery of hydrogel materials to living tissue has been achieved in several ways, including direct implantation of the material to the target site after formation during surgical procedures (Grover, Braden, and Christman 2013, 2940). Other methods have become progressively less invasive, ranging from catheter delivery to the injection of the polymer components directly to deliver the material to the region of interest within the body (Grover, Braden, and Christman 2013, 2939). Previous work has demonstrated the use of catheters to deliver hydrogel materials to the heart tissue for applications in tissue repair post-myocardial infarction. This is particularly noteworthy due to the use of an oxime-bonded hydrogel in this

study (Grover, Braden, and Christman 2013, 2940). However, while these techniques are advantageous for the precise transfer of a material to a specific area, they are not well-suited for the delivery of a uniform barrier over a relatively wide surface of tissue. In addition, the oxime-bonded material demonstrated during the earlier catheter studies demonstrated much slower kinetics compared to the new Ald-AO-DOPA gel, which forms between 2-3 s due to a different chemical formulation (Grover, Braden, and Christman 2013, 2939). Normal catheter or injection-based delivery, therefore, would be problematic due to close proximity of the two solutions inside the device.

Another method that is widely used in surgical procedures for material delivery is the process of atomization of the liquid solution into droplets facilitated by an air-driven spray. During this process, liquid is typically driven by an applied pressure, which in this case results in air flow, through an enclosed tubular region followed constricted space, or nozzle, open to an environment at atmospheric pressure on one side. During this phase, the flow of air is considered to be "choked" within the nozzle and reaches high velocities while simultaneously experiencing a decrease in pressure as the liquid phase undergoes breakup into ligaments or droplets, the latter being the primary focus of this study (Miller and Butler Ellis 2000, 610; ANSYS Inc. 2016, 13, 454). In the case of a number of spray-based devices used today, this two-phase transport of fluids can be achieved by the injection of liquid into the path of airflow or by the Venturi effect, which occurs when the lower pressure produced by choked air flow results in the travel of fluid from an orifice connected to the narrow region. In each method, liquid spray can be easily transferred from a source in order to achieve atomization (Joshi et al. 2011, 1).

When using an air assisted device, it should be noted that the use of a gas-assisted delivery system includes certain risks that must be taken into account when operating. In

particular, the improper use of gas during application has been known to result in unintended surgical complications such as embolism formation, the entrapment of gas within the body, and even damage to healthy tissue (Ebner et al. 2011, 180–81). These issues can arise due to excessive pressure from the air source combined with the use of a shorter operating distance between the tissue and the device head. Most products, for example, designate a maximum operating pressure of 25 psi and a minimum working distance of 10 cm from the patient (Chaurasia et al. 2012, 3). Therefore, when designing a new device, these limits are considered to be additional constraints during both testing and simulation.

The use of air- or pressure-assisted spray for biomaterial delivery in medical practices is not uncommon. Multiple products currently use this method for the delivery of biomedical substances, particularly sealants, as a reliable aid to healing and wound closure during surgery. The FibriJet applicator assembly from Nordson Medical is one example of this, and was used in earlier *in vivo* studies during evaluation of the Ald-AO-DOPA gel for adhesion prevention. This device is equipped with two separate paths for multiple solutions that can be delivered by syringe before being ejected by a filtered air source connected to the body of the device, which produces larger droplets when fluid is dispensed (Fujita et al. 2018, submitted). This is sufficient for experiments using murine models due to the smaller geometry of the device itself and the low surface area of the exposed rat heart during surgery. However, when working with large animal models or clinical studies, this method of delivery would be inadequate to ensure gelation of the material across the entire surface of the heart. Other options such as TISSEEL by Baxter Medical include pressure-driven delivery systems that are equipped to support multiple components to be delivered using a finer spray. However, these devices also allow the solutions used to mix prior to delivery due to longer required gelation times (TISSEEL 2017, 3).

In order to develop a device designed to deliver a fast-gelling multicomponent hydrogel, this study will focus on the implementation of a delivery method that includes two separate channels for the device that allow individual atomization of the two polymer solutions that make up the Ald-AO-DOPA gel while also ensuring sufficient mixing and gel formation upon delivery. This method of combined spray has been previously explored through the study of intersecting sprays impinging on a defined surface (Dohmann 1998, 342). A key feature of both this method and the design proposed here is that the two sprays must overlap so that equal delivery of both component solutions, in this case PEG-AO and PEG-Ald/PEG-DOPA, can occur. The trajectories of each spray can be predicted using computational models to simulate the trajectories of droplets dispersed by air flow. Additionally, final gel formation by the device can be validated by physical testing of the design to verify that crosslink formation and optimal mechanical properties are retained. In the context of this study, this will be achieved by integrating two individual methods of fluid flow into the development and evaluation of two novel prototypes.

Methods

Design of Initial Prototype

The primary feature of both the initial and final prototypes tested in this study is the incorporation of two intersecting sprays made from both the PEG-Ald/PEG-DOPA and PEG-AO polymer solutions. As an initial proof of concept, the first prototype incorporated two commercially purchased airbrushes that were connected to an electric air compressor with a maximum working pressure of 58 psi and 1/6 horsepower. The two individual units were linked to the compressor using two identical air hoses each 1.83 m long. The airbrushes themselves were originally designed such that a central nozzle for air flow is fixed adjacent to a second

nozzle connected to a liquid source in order to induce a Venturi effect to create atomized spray. In order to join both airbrushes together, a special link was designed to set both devices at an 8° angle inwards towards one another. Additionally, two custom-made caps were designed to fit two 4.5 mL vials for housing either polymer solution which were then attached to either of the two devices to be sprayed. Both caps and the link between the devices were designed on SolidWorks and printed using a Prusa i3 MK2 3D printer with PLA filament. This iteration is referred to here as Design 1.

Figure 3.1: Images of Design 1 prototype.

It should be noted that Design 1 was used during an *in vivo* porcine study after preliminary testing to deliver the Ald-AO-DOPA gel to the heart surface after abrasion. The results of this trial showed that adhesions were not prevented by addition of the material, despite gel delivery by the device. However, impaired spray by the unit housing the PEG-Ald/PEG-AO solution was also observed in this case, which may have resulted in an inadequate layer of material on the heart surface. Therefore, further modeling and testing of this device is necessary to develop a superior design.

Design of Final Prototype

The second and final prototype designed for this study incorporates the use of a branching path for air flow found in the original design into a single, smaller unit. Compressed air is applied directly by the compressor to an inlet 3.4 mm in diameter opposite the two nozzles

as seen in the figure below. Within the device itself, a forked pathway 4 mm in diameter forms two routes each 5.5 cm in length. A separate piece, designed to fit onto the main air source attachment, accommodates two individual 10 mL syringes to inject both PEG-AO and PEG-Ald/PEG-DOPA solutions into identical cylindrical pathways each 4.54 cm in length. Each of these begin with a portion of the route 2.8 cm long and 4 mm wide, followed by a narrowed region 1.74 cm long and 2 mm wide. Within this design, fluid injected through the lower attachment exits through the equipped nozzle heads adjacent to the second pair of nozzles attached to the main device body, where the flow of air is directed. In this way, each solution is directly delivered to the central path of air flow. Nozzle heads were purchased commercially, while all additional parts were designed in SolidWorks and made using a Prusa i3 MK2 3D printer with PLA filament. This iteration is referred to here as Design 2.

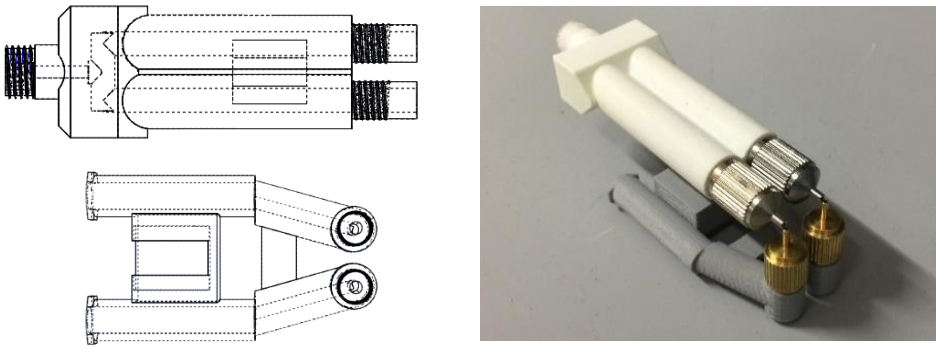

Figure 3.2: Images of Design 2 prototype. The images at the left display a transparent model as designed in SOLIDWORKS.

Single-Phase Air Flow Simulation

The COMSOL Multiphysics modelling software is used here to simulate the behavior of air flow within both devices. The compressor used in physical testing of the device is a standard electric unit capable of supplying an air flow of 0.5 cfm, or 2.35×10^{-4} m^3/s, at 20 psi working pressure. Using principles derived from Boyle's Law, the air flow from the compressor at

varying pressures can be calculated as seen in the equation below (Griffith 2016, 95, 102). For each prototype, only the pressure required to generate a visibly fine spray was considered during testing. In the cases of Design 1 and Design 2, these pressures were 16 psi and 8 psi, respectively. The dimensions of each geometry, based on the length and width of each of the channels within the body of each device, were modeled in a two-dimensional axisymmetric geometry.

$$(1)\ P_1 Q_1 = P_2 Q_2$$

For the Design 1, using a pressure of 16 psi, we calculated an air volume flow rate of 2.94×10^{-4} m^3/s at the compressor outlet. Pressure loss normally occurring through connecting air hoses is considered negligible, and the airflow is assumed to be halved in each branching pathway. Therefore, for channels 4 mm in diameter in each unit, the input velocity of the initial prototype is equal to 3.05 m/s. In this model, although only air flow is considered here, we assume a nozzle length and diameter of 5 mm and 0.5 mm with a separate branching outlet of equal width immediately at the mouth of the nozzle to represent the adjacent nozzle connected to a liquid source. An additional square region with boundaries of 4 mm immediately following the two nozzles is also modeled here to represent the open space outside of the device. In COMSOL, this geometry is created in a two-dimensional axisymmetric setup in order to account for the two separate units as part of a steady-state, or stationary, study. The density (1.23×10^{-3} g/cm^3) and dynamic viscosity (1.84×10^{-5} kg/m·s) of air are considered here as material properties of the fluid.

The inlet for the imposed air flow is defined 1 cm upstream of the nozzle using the velocity for each unit determined above. Outlets are defined with velocities and pressures of 0 m/s and 0 Pa at the opening of space following the nozzle as well as at the end of the liquid path

not in contact with the rest of the device. A no-slip condition is established at the walls defined as the nozzle body. Laminar flow is considered here and is characterized by the Navier-Stokes and continuity equations for incompressible flow (ANSYS Inc. 2016, 370). One-dimensional line plots across the width of the device body and the mouth of the adjacent nozzle for fluid flow were measured to determine the velocity of air in either region.

$$(2)\quad \rho v \frac{\partial v}{\partial x} = 0$$

$$(3)\quad \frac{\partial}{\partial x}\left(-pI\frac{\partial v}{\partial x} + \mu\frac{\partial v}{\partial x} + (\nabla v)^T\right) + F\rho\frac{\partial v}{\partial x} = 0$$

The modeling process in COMSOL for the second prototype is comparable to the first. Using Boyle's law again with a working pressure of 8 psi, the resulting air flow was found to be 5.88×10^{-4} m^3/s, which gives an air velocity of 16.3 m/s at an inlet 3.4 mm in diameter. As with the first device, adjoining nozzles for both air and fluid flow were modeled as intersecting regions 0.5 mm in diameter, with an additional square region with 4 mm sides representing the exterior of the device. Outlets designated at the far region of this added space and the opposite end of the nozzle for solution injection are defined with having boundary conditions of 0 Pa and 0 psi. A no-slip boundary condition was set at the inner walls of the device. Steady-state laminar flow is modelled here once more using the governing equations above.

After computation using the parameters given, the velocity profiles of both the device bodies were measured. The resulting profile can be used to calculate the average velocity, v_{ave} of air in the pipe assuming fully-developed flow using the equation below. Here, v_{max} is equal to the maximum air velocity at the center of the channel (Munson et al. 2009, 391–92). The values of v_{ave} found for Design 1 and Design 2 are equivalent to v_{inj1} and v_{inj2}, which serve as the boundary conditions at the inlets during spray modeling for both droplet and air velocity.

$$(4)\quad v_{ave} = \frac{1}{2} v_{max}$$

Mathematical Principles of Spray Modeling

The behavior of liquid spray can be best described using multiple mathematical models that can be applied simultaneously within computational software to account for the transport of the two fluid phases that occurs during the formation of spray. Specifically, the flow of air both within and outside the device and the behavior of individual liquid droplets formed from either polymer solution must be taken into consideration. Due to the presence of turbulent air flow seen in this type of delivery, one can determine part of the fluid behavior using a model that considers the turbulent kinetic energy *k* as well as its dissipation rate $\mathcal{E}$ (ANSYS Inc. 2016, 51). The most useful of these models is known as the realizable turbulent k-Ɛ model. The realizable model is considered to be best suited to describing turbulent flow because of its inherent constraints on Reynolds stresses as well as its superior characterization of Ɛ and viscosity of eddies in air flow through modified formulae. This method is considered to be one of many sets of Reynolds-averaged Navier-Stokes equations, which account for the continuous fluid phase of the simulation. The governing transport equations for this model consider k and Ɛ through the use of partial differential equations, presented below (ANSYS Inc. 2016, 51).

$$(5)\quad \frac{\partial}{\partial t}(\rho k) + \frac{\partial}{\partial x_j}(\rho k v_j) = \frac{\partial}{\partial x_j}\left[\left(\mu + \frac{\mu_t}{\sigma_k}\right)\frac{\partial k}{\partial x_j}\right] + G_k + G_b - \rho\varepsilon - Y_M + S_k$$

$$(6)\quad \frac{\partial}{\partial t}(\rho\varepsilon) + \frac{\partial}{\partial x_j}(\rho\varepsilon u_j) = \frac{\partial}{\partial x_j}\left[\left(\mu + \frac{\mu_t}{\sigma_\varepsilon}\right)\frac{\partial \varepsilon}{\partial x_j}\right] + \rho C_1 S\varepsilon - \rho C_2 \frac{\varepsilon^2}{k+\sqrt{v\varepsilon}} + C_{1\varepsilon}\frac{\varepsilon}{k} C_{3\varepsilon} G_b + S_\varepsilon$$

Here, ρ and μ represent the density and viscosity of the fluid, respectively, while C_2 is a constant and C_1 is the maximum value between 0.43 and another value determined by *k*, $\mathcal{E}$ and spin parameter *S*. The values σ_ε and σ_k represent the Prandtl numbers for both *k* and $\mathcal{E}$, and are

calculated based on the ratio of the diffusion rates due to viscosity and thermal effects for each quantity (ANSYS Inc. 2016, 52, 53). Both Prandtl numbers, as well as the designated constants, are experimentally determined values that are well-established for this model and are presented in the table below.

Table 3.1: Constant terms used during calculations for the realizable k-Ɛ turbulence model as determined by previous experimentation.

Table 3.1: Turbulence Model Constants	
Symbol	Value
C_2	1.9
σ_ε	1.0
σ_k	1.2

For the purposes of this study, equations (5) and (6) are simplified such that the effects of turbulence due to buoyancy characterized by G_b are not considered. Buoyancy effects occur in the presence of both gravity and a temperature gradient, the latter of which is not present in this simulation. Additionally, the user-defined generation terms S_k and S_ε were also not considered here, giving equations (7) and (8) as final expressions for turbulent kinetic energy and its dissipation rate, respectively. Both expressions were used for modelling each iteration of the device (ANSYS Inc. 2016, 53).

$$(7) \qquad \frac{\partial}{\partial t}(\rho k) + \frac{\partial}{\partial x_j}(\rho k u_j) = \frac{\partial}{\partial x_j}\left[\left(\mu + \frac{\mu_t}{\sigma_k}\right)\frac{\partial k}{\partial x_j}\right] + G_k - \rho\varepsilon - Y_M$$

$$(8) \qquad \frac{\partial}{\partial t}(\rho \varepsilon) + \frac{\partial}{\partial x_j}(\rho \varepsilon u_j) = \frac{\partial}{\partial x_j}\left[\left(\mu + \frac{\mu_t}{\sigma_\varepsilon}\right)\frac{\partial \varepsilon}{\partial x_j}\right] + \rho C_1 S\varepsilon - \rho C_2 \frac{\varepsilon^2}{k+\sqrt{\nu\varepsilon}}$$

In equations (5) and (7), the term Y_M represents the influence of fluid compressibility on turbulence in the system. In these same formulae, G_k denotes a generation term for turbulent kinetic energy in the system based on gradients in the average velocity while μ_t denotes the eddy

viscosity, each of which are defined by the expressions below. In the case of the realizable k-Ɛ model, C_μ is a variable term computed from strain and rotation tensors (ANSYS Inc. 2016, 52–54).

$$G_k = \mu_t S^2 \tag{9}$$

$$\mu_t = \rho C_\mu \frac{k^2}{\varepsilon} \tag{10}$$

When analyzing the distribution of liquid droplets as a fine spray, a widely-used method of simulating this process is performed in terms of a continuous phase, represented by the air flow, while considering a separate "discrete" phase of droplets as distinct particles rather than as a flowing liquid. This concept is known as the discrete phase model, which allows users to find a numerical solution using appropriate mathematical principles and experimentally determined values (ANSYS Inc. 2016, 381). Computation of each part of the model involves mathematical simulation of the continuous and discrete phases through Eulerian and Lagrangian models, respectively. The fluid phase is described by the realizable turbulent k-Ɛ model discussed above to account for deviations from laminar flow experienced outside the device (ANSYS Inc. 2016, 381).

When applying the Lagrangian method to model droplet behavior, transport equations can be used to determine particle trajectories. These are typically present in the form of a force balance between the inertia of individual droplets and other acting forces, as shown in the ordinary differential equation given in (11). Note that the first two terms in this form denote the forces due to drag and gravity, the latter of which is dependent on gravitational acceleration g. The additional generation term on the right hand side can be expanded to include other forces

acting on individual particles. Only the force due to the lifting of rotating particles, known as the Magnus lift force, will be discussed here (ANSYS Inc. 2016, 382).

$$\frac{dv_p}{dt} = \frac{\overrightarrow{v_p} - \vec{v}}{\tau_p} + \frac{\vec{g}(\rho_p - \rho_f)}{\rho_p} + \vec{F} \tag{11}$$

During motion, individual droplets can experience rotation when transported together with a fluid. In order to account for this in the proposed model, the relationship below can be used. Here, *I* denotes the particle's moment of inertia, considering a spherical particle as given in (12). The values ρ_p and d_p represent the particle density and particle diameter, respectively (ANSYS Inc. 2016, 382).

$$I = \frac{\pi}{60}\rho_p d_p^5 \tag{12}$$

By considering the effects of particle rotation, this model also includes the Magnus lift force into (11). The magnitude of this force *M* is given below, where $\vec{V}$, *A*, and C_r are equal to the particle velocity relative to the fluid phase and particle surface area, respectively. The value $\overrightarrow{\omega_0}$ denotes the angular velocity of the particle relative to the fluid phase (ANSYS Inc. 2016, 345).

$$M = \frac{1}{2} A C_r \rho_f \frac{|\vec{V}|}{|\overrightarrow{\omega_0}|} (\vec{V} \times \overrightarrow{\omega_0}) \tag{13}$$

This simulation will utilize the Rubinow-Keller definition of lift force, which is characterized by a value of C_r as shown below, where S_p denotes the spin parameter computed from the velocity and angular velocity of the particle and the velocity of the fluid phase (ANSYS Inc. 2016, 386).

$$C_r = 2S_p \tag{14}$$

In order to solve (11) over time, one can use implicit Eulerian discretization, or "backwards" discretization, in order to solve for the trajectory of the particles at each point in time. This is done by considering the difference between the trajectories at the following time point and at the time point being calculated. The modeling program ANSYS Fluent incorporates this method for numerical modeling purposes, which will serve as a basis for this simulation. According to this technique, (11) can be simplified into the form given in (15), which includes the acceleration term *a* for all additional forces considered in the simulation (ANSYS Inc. 2016, 392).

$$\frac{dv_p}{dt} = \frac{1}{\tau_p}\left(v_p - v\right) + a \tag{15}$$

In order to perform backwards discretization, one assumes an expression for v_p^{n+1} of the form given in (16). Taking (15) as a function of v_p^{n+1} and v^n and substituting into this new relationship, a new expression for v_p^{n+1} can be derived as shown below (ANSYS Inc. 2016, 392).

$$\frac{v_p^{n+1} - v_p^n}{\Delta t} = \frac{1}{\tau_p}\left(v^n - v_p^{n+1}\right) + a \tag{16}$$

$$v_p^{n+1} = \frac{\Delta t\left(\frac{v^n}{\tau_p} + a\right) + v_p^n}{\left(\frac{\Delta t}{\tau_p} + 1\right)} \tag{17}$$

The general expressions for determining particle trajectory thus far can be applied further in order to determine particle motion in the case of turbulent flows. The ANSYS Fluent software can be used to calculate this behavior using either particle cloud tracking or stochastic particle tracking. The former method involves utilizing a Gaussian function to determine an averaged trajectory for all particles in order to model the effects of divergence. By contrast, stochastic particle tracking involves integration of the equations of motion to determine individual trajectories of each particle based on the velocity of a particle at a given instant, *v(t)*, as presented

in (18), where $\bar{v}$ denotes the average velocity of the fluid phase. Changes in this velocity can be accounted for by using the discrete random walk (DRW) model. This method of tracking is performed by integrating over a time step characterized by particle velocity as well as an additional time step used in the instance of particles that move with the fluid phase itself (ANSYS Inc. 2016, 386-387).

$$v(t) = v_{ave} + v'(t) \tag{18}$$

The deposition of droplets onto the tissue surface can be approximated based on statistical analysis. This approach yields more accurate trends in droplet location compared to a uniform model, in which droplets are assumed to be evenly distributed across an area. A Gaussian distribution is typically assumed due to the cone of spray beginning at each nozzle of the device, with the largest number of particles being deposited at the center of the cone while as droplet frequency decreases radially with distance (Stepanenko 2007, 2567). The actual deposition of each solution at a certain distance, in this case at the outlet, for each model can be determined via particle tracking.

Discrete Phase Modelling

Model geometries were prepared and exported from Solidworks. For both designs, nozzle bodies were modeled as cylinders 4 mm in diameter, while the tips 0.5 mm in diameter connect the nozzle to a larger geometry to represent open space. During meshing, the base of the nozzle bodies are designated here as two distinct inlets, each 4 mm in diameter for the entry of air and component solutions of the hydrogel. In the case of Design 1, each nozzle is set at an 8° angle inwards towards the other with the nozzle heads positioned 1.95 cm from each other. In Design 2, the nozzle bodies are placed immediately next to one another at one end of the geometry, so

that the nozzle openings into the larger portion of the model are placed only 0.95 cm apart. At the end of each geometry opposite the nozzle heads, an outlet 7 cm wide was defined to represent the tissue surface at a certain distance from the nozzle. For each design simulated, distances of 10 cm, 12.5 cm, 15 cm, and 20 cm from the end of each nozzle were used to simulate different operating distances.

Before beginning the modeling process in ANSYS Fluent, the mesh was converted to a polyhedral geometry. For this simulation, a pressure-based solver was used, due to its accuracy at a range of Mach numbers, and applied to a steady-state model. The acceleration due to gravity was specified in the y-direction alone and given a value -9.81 m/s^2. A steady-state solver was used for both the continuous and discrete phases, such that the change of variables with time was set equal to zero. The realizable k-Ɛ turbulence model was enabled along with enhanced wall treatment, which allows computation of values including turbulent viscosity, kinetic energy and momentum in the region near the wall based on meshing. Enhanced wall treatment is generally recommended for modeling with the realizable k-Ɛ method.

In order to increase computational efficiency, the influence of particles on air flow was not considered. Two separate injections were set to account for both PEG solutions, and were each defined as inert particles with distinct densities equivalent to the densities of each solution, ρ_{AO} and $\rho_{Ald/DOPA}$, which were calculated based on measurements of mass and volume taken from each solution. Each set injection began at the inlets defined during meshing, across the area of each surface, and discrete phase particles for both inlets were assumed to have an injection velocity normal to this area of either v_{inj1} or v_{inj2} for Design 1 or Design 2, respectively. These values are equal to the air velocity determined in single-phase simulation. In each case, the injection velocity is assumed to be equal to the flow of air and therefore is equal to the velocity

computed during single-phase air flow measurements. These values, together with the nozzle dimensions and the solution densities, are used to calculate $\dot{m}_{AO1}$, $\dot{m}_{DOPA1}$, $\dot{m}_{AO2}$, $\dot{m}_{DOPA2}$ for both Design 1 and Design 2. These parameters, along with others, are listed in the table below. The Magnus lift force, which considers the lift generated by rotation of individual parcels was activated in this model as well, with an initial angular velocity of 0 rad/s. This is accompanied the activation of Magnus lift force within ANSYS Fluent as proposed by Rubinow and Keller. A spherical drag law for each particle was considered here, and the discrete random walk model was enabled. The injected particles are assumed to be non-uniform in size according to the rosin-rammler distribution of diameter, which assumes droplet diameters ranging from 2 μm to 200 μm based on the range reported for fine sprays (Spraying System Co. 2000, 1–2).

Boundary conditions for both nozzles were defined as velocity inlets using the computed air velocities from the steady-state COMSOL model. These surfaces were also designated with an "escape" boundary condition for injected particle. This was value was also used along with the hydraulic diameter d_{hd} (0.004 m) to calculate the Reynolds number, Re_{hd}, for the hydraulic diameter and turbulence intensity T for each design as shown in the calculations below, where κ_{air} (1.5×10^{-5} m^2/s) denotes the kinematic viscosity of air.

$$Re_{hd} = \frac{v_{inj} d_{hd}}{\kappa_{air}} \tag{19}$$

$$T = 0.16 Re_{hd}^{-\frac{1}{8}} \tag{20}$$

The walls of the nozzle served as a reflective boundary in this model and were assigned no-slip conditions. The walls of the space outside the defined nozzle body, except for the outlet, served as trap boundaries for the discrete phase, reducing the velocity of these particles to zero. A velocity outlet was given a gauge pressure of zero and as well as both a turbulent backflow

intensity and hydraulic diameter defined by the width of this region. The outlet was also given an escape boundary condition for exiting particles. The computation was initialized from all regions within the geometry, computing initial values for turbulent kinetic energy and its dissipation rate automatically.

Absorbance Spectroscopy

Preliminary mixing studies were performed using aqueous dye solutions within the separate channels of the device. Blue and yellow dyes were added to deionized water (1:8, v/v) to make two distinct solutions. White sugar was added to the blue solution (1.067 mg/mL) to produce a viscosity similar comparable to that of the PEG-Ald/PEG-DOPA solution (0.04 Pa·s). The yellow solution was not treated with additional solutes due to the relatively low viscosity of the PEG-AO solution, 0.01 Pa·s. Viscosities were calculated using an AR G2 parallel plate rheometer. Both solutions were added 1:1 (v/v) to form 500 µL of green solution in a 24-well plate which was analyzed using UV-vis absorbance scanning on a TECAN plate reader to determine a standard spectrum for the green solution. The resulting signals indicate absorption maxima for both blue (630 nm) and yellow (420 nm), such that a green solution appears as an intermediate between the two. Each device was used multiple times (n=5) at working distances of 10 cm, 12.5 cm, 15 cm, and 20 cm from a Petri dish 5.5 cm in diameter. After each trial, 500 µL of the resulting solution was collected and measured for absorbance at 420 nm and 630 nm.

FTIR Spectroscopy

A volume of 1 mL of both PEG-AO and PEG-Ald/PEG-DOPA solutions was prepared for both prototypes. Each device was operated 15 cm away at a trajectory perpendicular to a Petri dish 5.5 cm in diameter. After being allowed to dry for 5 minutes, material produced by each

device was then collected and placed into separate 15 mL Falcon tubes before freeze-drying on a lyophilizer overnight. Additionally, 100 µL of hydrogel was prepared by pipetting under otherwise identical conditions for comparison. Samples were then collected and analyzed via FTIR spectroscopy, using an empty stage as a background. The spectra produced were then studied for the presence of oxime bonds based on characteristic peaks of the material produced by each prototype.

Parallel-Plate Rheometry

The mechanical properties of Ald-AO gels produced by Design 2 (n = 3) were determined using rheological testing using an AR G2 parallel-plate rheometer. Gels from both were sprayed onto individual Petri dishes covered in Parafilm using 1.5 mL of both PEG-AO and PEG-Ald/PEG-DOPA solutions to form a complete layer before incubating at room temperature. At set time points of 15 minutes and 3 hr, samples of the gel were taken from each dish and measured for storage moduli at 37 °C under a frequency sweep ranging from 10^2 Hz to 10^{-2} Hz with 0.3 N normal force.

Statistical Analysis

Two-way ANOVA ($p < 0.05$) was used to determine the significance of the results of the solution mixing trials between both the variables of spraying distance and absorbance wavelength. Analysis of the material retention assay results was performed using one-way ANOVA and post hoc Tukey's test as discussed previously.

Results

Single-Phase Air Flow Modelling

By modeling fluid flow through the geometry of the device, the values obtained for air velocity can be used as inputs for modeling the final spraying process from the device. The air flow simulation for the original in the velocity profiles shown below show a maximum of 6.13 m/s in the body of the prototype using an inlet velocity of 3.82 m/s calculated from a working pressure of 16 psi. This allows users to determine the average velocity within the body of each unit assuming the flow is fully developed, yielding the values presented in Table 2.2. This value is presented in the table below. As indicated in the figure below, a Venturi effect is formed at the intersecting channel near the nozzle exit, reaching a maximum velocity of 5.41 m/s directed towards the central path of air flow. As shown in the curve below, air velocity obtained in the body of Design 2 with an inlet velocity of 16.28 m/s, achieved using 8 psi working pressure, produced a maximum of 0.75 m/s. Assuming again that the flow is fully-developed, the average velocity can be calculated in the same manner as that found in Device 1. The average velocities obtained through each of these were subsequently used as boundary conditions for discrete phase modelling for both discrete and continuous phases. From these values, additional parameters including mass flux and turbulent intensity were calculated to give the values shown in Table 2.3.

Table 3.2: Values of Single-phase air velocity as computed through COMSOL Multiphysics assuming fully-developed laminar flow.

Table 3.2: Computed Values for Air Velocity		
	Max. Velocity (m/s)	Mean Velocity (m/s)
Design 1	6.13	3.07
Design 2	0.750	0.375

Table 3.3: Calculated values from results of single-phase modelling used as inputs for discrete phase modeling with ANSYS Fluent.

Table 3.3: Input Values for Discrete Phase Modelling	
Parameter	Value
v_{inj1}	3.067 m/s
v_{inj2}	0.375 m/s
$\dot{m}_{AO1}$	0.0385 kg/s
$\dot{m}_{AO2}$	0.005 kg/s
$\dot{m}_{DOPA1}$	0.0573 kg/s
$\dot{m}_{DOPA2}$	0.007 kg/s
Re_{hd1}	817.9
Re_{hd2}	100
T_1	6.9 %
T_2	8.9 %

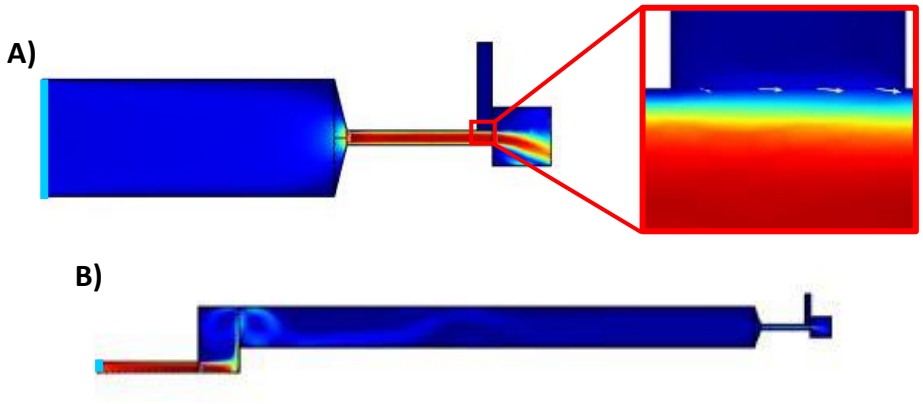

Figure 3.3: Solution graphics of single-phase air flow behavior seen in both Design 1 (A) and Design 2 (B). A slight Venturi effect can be seen in the magnified portion of (A). Air flow in both models is directed from left to right from the inlet marked by the blue border. Gradients from blue to red indicate an increase in air velocity.

Discrete Phase Model Simulation

The general trajectory of each spray and constituent droplets can be visualized via particle tracking taken from the steady-state solution as shown below, demonstrating the general "cone" of spray produced by each nozzle. Here, the predicted sprays at 20 cm from both designs are shown as a representative of the trajectories over the maximum distance. The average location of particles from either spray used is represented in the table as a mean ± standard

deviation. The deposition of particles at the outlet is plotted as shown by determining the frequency of droplets deposited into one of three "bins" of equal width, 2.333 cm each, over the span of the 7 cm. After 100 iterations, both Design 1 and Design 2 have the greatest amount of deposition in the central region of this defined range, between 2.333 cm and 4.667 cm, over all distances tested. The predicted deposition of Design 1, when considering the ratio of PEG-AO to PEG-Ald/PEG-DOPA solution particles, is approximately 6:5 at distances of 10 cm, 12.5 cm, and 15 cm. This ratio shifts towards greater deposition of PEG-AO particles in this region at a working distance of 20 cm, increasing to 3:2. As shown in the table, Design 2 demonstrates particle ratios that are more closely deposited in a 1:1 ratio. Similarly to Design 1, however, the type of particles delivered are skewed towards the PEG-AO solution at 20 cm, with the ratio increasing to 4:3.

Graph 3.1: Deposition of PEG-AO and PEG-Ald/PEG-DOPA for Design 1 over different working distances. PEG-AO is represented by the yellow columns, while PEG-Ald/PEG-DOPA is represented by the blue columns.

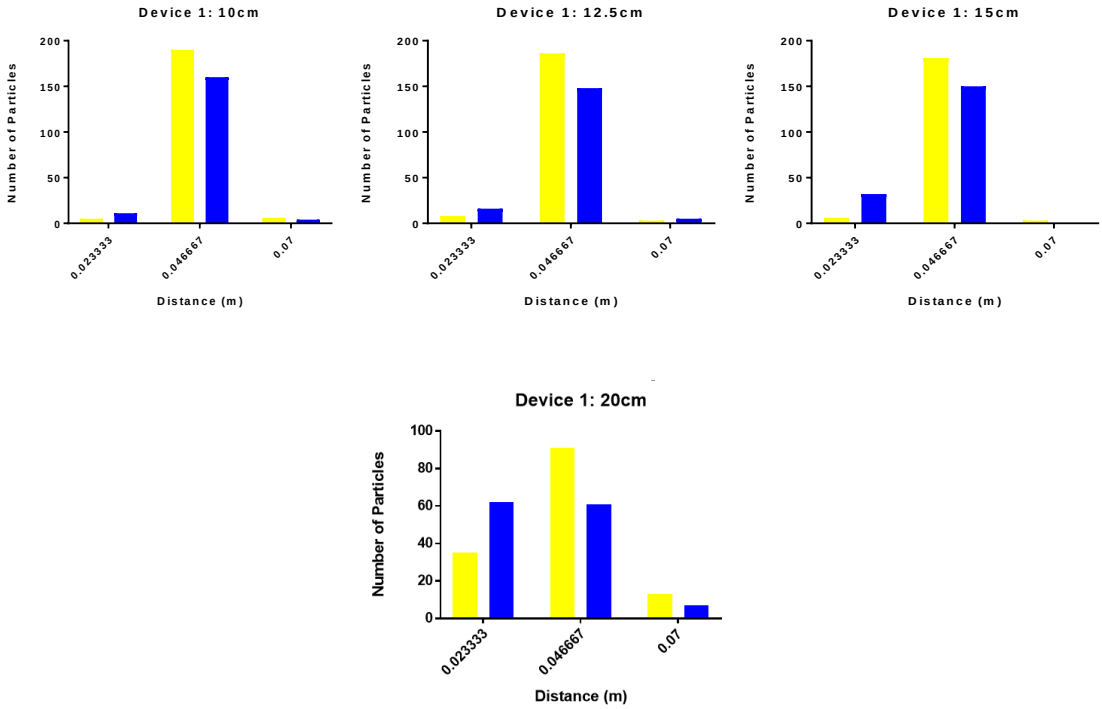

Graph 3.2: Deposition of PEG-AO and PEG-Ald/PEG-DOPA for Design 2 over different working distances. PEG-AO is represented by the yellow columns, while PEG-Ald/PEG-DOPA is represented by the blue columns.

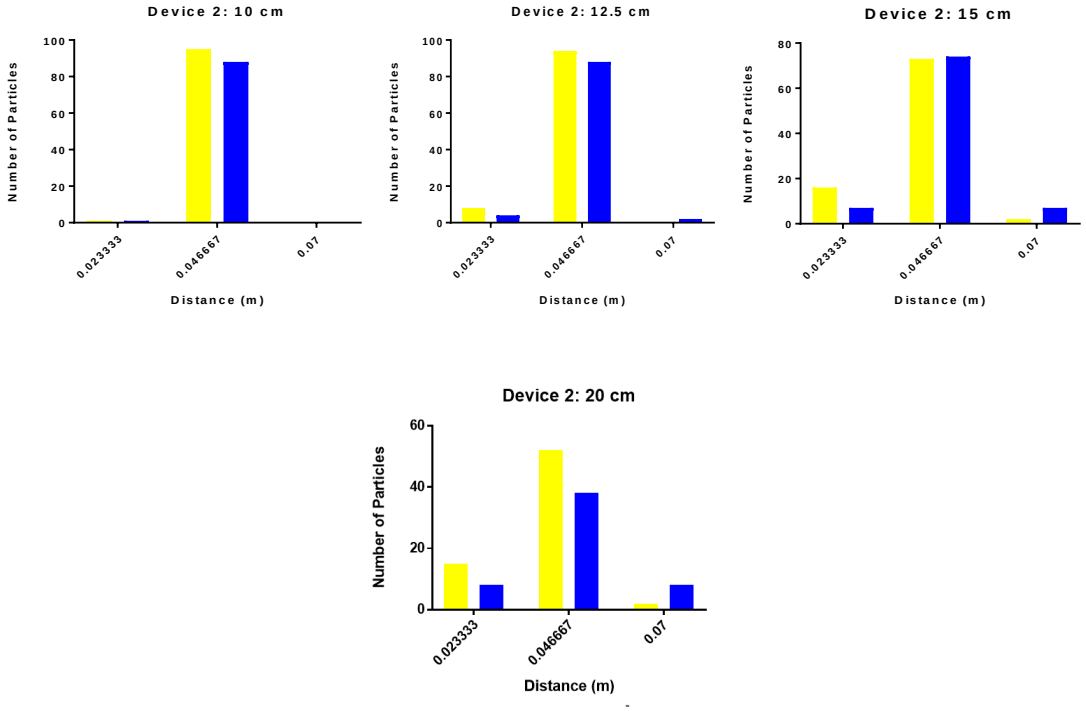

Table 3.4: Average particle deposition of both component solutions using each design. Values are given as mean ± standard deviation.

Table 3.4: Particle Deposition		
Design 1		
Distance	PEG-AO	PEG-Ald/PEG-DOPA
10 cm	0.03520 ± 0.006	0.03433 ± 0.006
12.5 cm	0.03476 ± 0.006	0.03419 ± 0.007
15 cm	0.03588 ± 0.006	0.03268 ± 0.010
20 cm	0.03221 ± 0.012	0.02658 ± 0.011
Design 2		
Distance	PEG-AO	PEG-Ald/PEG-DOPA
10 cm	0.03167 ± 0.003	0.03668 ± 0.003
12.5 cm	0.03184 ± 0.005	0.03737 ± 0.006
15 cm	0.03110 ± 0.008	0.03706 ± 0.008
20 cm	0.02907 ± 0.011	0.03771 ± 0.011

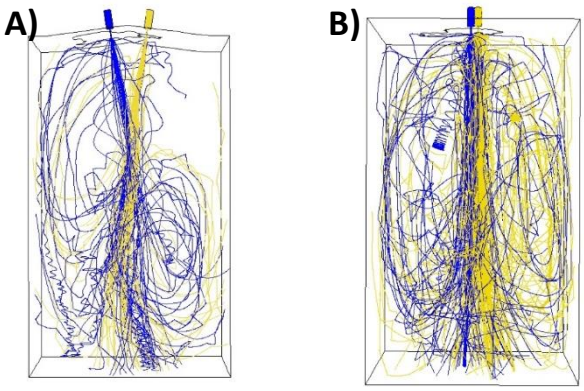

Figure 3.4: Graphic representation of particle trajectories from (A) Design 1 and (B) Design 2. Particle tracking was performed for a simulation of 20 cm working distance. Yellow and Blue denote the PEG-AO and PEG-Ald/PEG DOPA solutions, respectively.

Solution Mixing

Testing of both devices for 1:1 mixing of both polymer solutions using absorbance spectroscopy at increasing distances yielded the results shown in the figure and tables below. Standard absorbance readings at 420 nm and 630 nm were measured at 1.61 ± 0.872 and 1.48 ± 0.834, respectively. Testing of Design 1 for each distance shows a large amount of dyed yellow solution present compared to the blue sugar solution sprayed. The largest of these differences occurs at a working range of 12.5 cm, which has an average absorbance reading of about 3.5 420 nm and 0.8 at 630 nm. Two-way ANOVA performed on Design 1 indicates significant variation between columns (****p < 0.0001).

Graph 3.3: Absorbance readings at 420 nm and 630 nm of substitute aqueous solutions dyed yellow and blue for both Design 1 (A) and Design 2 (B). The same standard was used for each case, and was prepared by pipetting equal volumes of both solutions as a control (n=5).

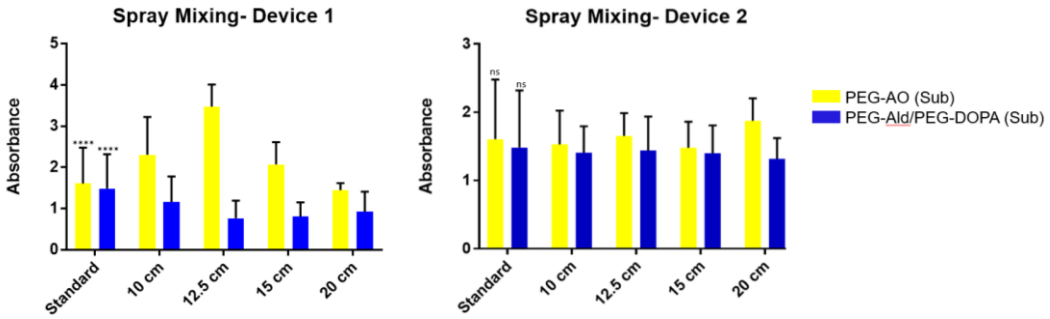

Table 3.5: Statistical data for absorbance spectroscopy from substitute aqueous solutions delivered by Device 1 and Device 2. Values are given as mean ± standard deviation.

Table 3.5: Absorbance Spectroscopy		
Design 1		
Distance	420 nm	630 nm
10 cm	2.31 ± 0.915	1.16 ± 0.618
12.5 cm	3.47 ± 0.536	0.77 ± 0.426
15 cm	2.07 ± 0.541	0.81 ± 0.345
20 cm	1.45 ± 0.169	0.92 ± 0.490
Design 2		
Distance	420 nm	630 nm
10 cm	1.53 ± 0.494	1.41 ± 0.387
12.5 cm	1.65 ± 0.332	1.44 ± 0.499
15 cm	1.48 ± 0.382	1.40 ± 0.408
20 cm	1.88 ± 0.328	1.32 ± 0.305

FTIR Spectrum Analysis

The use of FTIR allowed us to determine the presence of oxime bonds in the Ald-AO-DOPA material. The spectra produced from the gels formed with Device 1, Device 2, and the two pipe1ttes display the trends shown in the figure. In each of these, several significant peaks appear towards the lower end of the spectra with another large peak at about 2900 cm^{-1}. Most notably, each spectrum shows small peaks ranging from approximately 1600 cm^{-1} to 1750 cm^{-1}, which is indicative of the formation of oxime bonds.

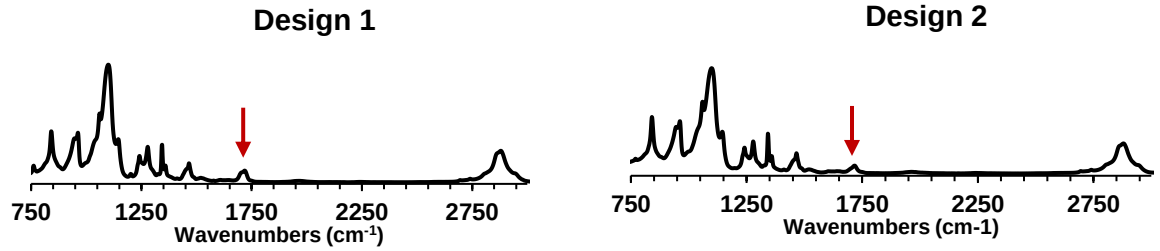

Figure 3.5: FTIR spectra taken from Ald-AO-DOPA gels formed by Design 1 and Design 2. Oxime bond peaks appear between 1600 cm^{-1} and 1750 cm^{-1} as indicated by the arrows.

Rheological Analysis

Measurements obtained using a parallel-plate rheometer can be compared with those taken from gel samples formed in earlier studies to determine whether the method of spray affects the mechanical properties of the material. Storage moduli obtained from parallel-plate rheometry performed on Ald-AO gel samples made with the Design 2 prototype were measured at 7089 ± 4329.91 Pa and 11335.67 Pa ± 6750.72 Pa after 0 hr and 3 hr of incubation, respectively. Statistical analysis was performed using an unpaired t-test and showed that the measurements obtained from both time points were not statistically significant from one another.

Graph 3.4: Storage moduli obtained from rheological studies of Ald-AO hydrogel formed by spraying. Values are reported as mean ± standard deviation.

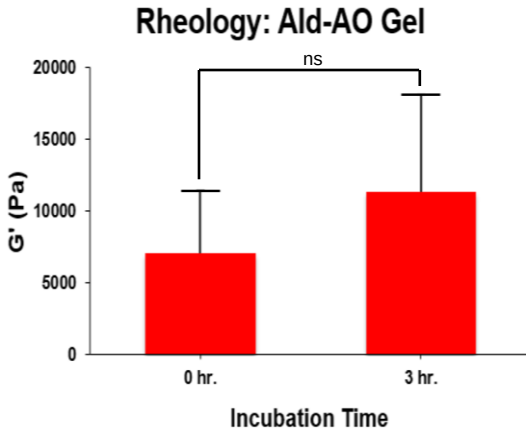

Discussion

The results of both the two-dimensional simulation of air flow and the three-dimensional model of liquid droplet dispersion indicate that delivery of the hydrogel by atomized spray is a viable option. Using simulations of the continuous fluid within the body of a device, parameters such as velocity can be computed and used as inputs when modeling the actual spray process. In the case of Design 1, this involves accounting for the branched air flow created by the two

existing devices connected to a single air source. Here, the process of steady-state laminar flow shows that pressurized air can be influenced by the geometry of the system using concepts of mass flow choking and the Venturi effect. This phenomenon is due in part to the inclusion of a square region with 4 mm sides at the opposite end of the nozzle assembly, representing the exterior space during spray. Due to the increase in air velocity within the nozzle, a significant amount of air flow can be observed from a channel adjacent to this rapid current that is capable of creating atomized spray during testing of the device. For both designs, the average velocities found represent a reasonable approximation of input parameters based on the principles outlined by fluid flow and gas laws.

The implementation of separate syringes in Design 2 provides an alternative method of fluid transport through applied pressure to the two plungers to deliver liquid to the main paths of air flow. For this reason, the Venturi effect is considered negligible in the new design. It is worth noting that despite a higher input velocity than in the original design, the air flow rate found in the main body of Design 2 is significantly lower than that in Design 1. This could be due in part to the branched geometry of the device for moving air, which can disrupt established laminar flow, as the velocity of air experiences a significant drop. Previous studies have reported satisfactory separation of flow in a 90° bifurcation such as the one modelled here with a less severe reduction in flow, but have used a different inlet relative to the intersection, which may account for this difference (Carr and Kotha 1995, 444). The effects of this disturbance are apparent in the boundary conditions of the discrete phase models, in which the turbulent intensity calculated at the inlets of Design 2 is significantly higher than that found for Design 1. Therefore, for future iterations of this device, it may be necessary to explore different geometries when designing the inner channels of the device designed for air flow.

The discrete phase model for spray distribution predicts the deposition of the two liquid components within close proximity of each other when using both Design 1 and Design 2. The expected cones of spray seen in existing devices of this nature is demonstrated qualitatively here based on the simulated trajectories of tracked particles in the steady state. This model also predicts that the imposed velocity of the particles is sufficient to transport each solution to a given surface over every distance tested. Deposition of the droplets at the outlet was analyzed in the horizontal direction only due to the alignment of the nozzles in both designs as well as a negligible amount of observed variance between the two sprayed solutions in the vertical direction. Additionally, the larger number of particles tracked at the outlet in Design 1 occurs as a result of the higher injection velocity set for both solutions. It should be noted that due to the establishment of a trap boundary condition at all surfaces except for the modeled nozzle walls and outlet, not all of the particles injected will contact the outlet, resulting in some discrepancies in sample size for each simulation.

The outcome of the discrete phase model shown demonstrates that the two solutions sprayed by both designs experience the maximum amount of deposition within the central region of the outlet. This reflects the non-uniform nature of particle dispersion by this method, as the frequency of droplets contacting the outer regions of this area is significantly reduced. In discrete phase simulations for Design 1, the ratio of the particles tracked in the center of the outlet for all distances indicates that this initial device results in a less favorable degree of mixing between the two solutions. By contrast, the nearly 1:1 ratio of PEG-AO and PEG-Ald/PEG-DOPA at 10 cm, 12.5 cm, and 15 cm suggests that favorable mixing occurs within these ranges. The skew seen at 20 cm in favor of the PEG-AO solution in this same area for both Design 1 and Design 2, along with a broader distribution in particle deposition seen in both cases, is likely due to the effects of

turbulence imposed on airborne droplets. However, unpaired t-test analysis of the average particle locations also shows that the difference between the distributions of PEG-AO and PEG-Ald/PEG-DOPA are statistically significant in all cases except at working distances of 10 cm and 12.5 cm when using Design 1. Therefore, while the model does validate that bulk deposition of droplets occurs in a defined area of a surface, it also maintains that the two sprays used are distinct from one another at a smaller scale.

The discrete phase simulation is ideal for this study because it considers the dispersion of fine droplets, rather than continuous fluid flow, that take up a minimal amount of the defined volume in the geometry (ANSYS Inc. 2016, 381). However, this method also employs multiple assumptions that must be considered when evaluating these results. For example, other studies modeling the behavior of intersecting spray trajectories incorporate measurements of collisions between individual airborne particles as a method of increasing the range of the combined atomized product (Dohmann 1998, 341–42). Despite this, in early working tests of both designs used here, this effect appeared to be negligible in practice and was not considered during the simulation. Second, the principle of the model itself, which states that droplets are approximated as solid particles of a certain size and density, does not take into account either the momentary liquid behavior of droplets on a defined surface or the chemical reactions occurring between polymers on this surface. Despite the rapid formation of crosslinks between components, the brief accumulation of liquid on the surface would facilitate additional mixing that cannot described by the discrete phase model. As a result, physical testing of either prototype is necessary in addition to the simulation of particle deposition in order to validate this method of delivery.

The spectrophotometric data taken from physical testing of each device indicate that mixing at a 1:1 ratio is achieved by Design 2 over a wide range of distances. At each point, the average absorption values at both 420 nm and 630 nm are comparable to those obtained by the standard, with no statistically significant difference occurring between each group. Even without the use of the final PEG-AO and PEG-Ald/PEG-DOPA solutions, these results indicate that Design 2 is a reliable method to deliver solutions with comparable physical properties in equal amounts, providing further validation as a working method of delivery. This also agrees with the results of the discrete phase modeling detailed above, which predicted a nearly equivalent placement of droplets within a significant portion of the sprayed area. By contrast, the readings taken from solutions made by Design 1 demonstrate that a significantly larger amount of the yellow, less viscous solution is delivered relative to the blue sugar solution. Despite this discrepancy, it is important to note that gel formation is still possible, as previous testing with oxime-bonded materials achieved gelation using different ratios of the component polymers (Grover et al. 2015, 1329). According to this same study, however, these formulations may also exhibit inferior mechanical and retention properties. The results obtained in this experiment for Design 1 also differ from the simulation results, which yield amounts of each solution within the central region that more closely follow the desired 1:1 ratio. This could be due to inherent mechanical issues with the device, specifically the use of two separate units with distinct pathways from the air source which may result in leaking from the airways. This would result in slight differences in air flow between the two units, which would lead to a lower rate of spray due to a decreased Venturi effect that is not accounted for during modeling, in which equal rates of flow are assumed.

The readings produced from FTIR spectroscopy indicate that a cohesive gel was formed successfully with both Device 1 and Device 2. Analysis of the spectra produced indicates that oxime bond formation occurs in both sprayed freeze-dried samples in the same manner as the material formed by pipette delivery. This demonstrates that gel formation can be performed using air-driven spray in addition to earlier delivery techniques relying on pipette use. In addition, the locations of the peaks ranging from 1600 cm^{-1} to 1750 cm^{-1} closely match those observed by Grover et al. (1329) in earlier studies of the Ald-AO hydrogel, showing that this same cross-linking behavior occurs in all samples tested. As the oxime bond formation is a vital component of the functioning material, this provides evidence of a working gel barrier.

Rheological testing was performed on hydrogel samples produced by Device 2 due to the favorable mixing and FTIR readings demonstrated in earlier trials. Mechanical testing was performed on Ald-AO due to its initial gelation kinetics, which are comparable to the Ald-AO-DOPA gel. Rheological studies demonstrate here that no significant change in the storage modulus occurred during the three-hour incubation period, which was reported in studies by Fujita et al. using material formed via pipette. The measured values of G' were approximately within the range of 10,000 Pa to 100,000 Pa, which corresponds to the mechanical properties of cardiac tissue (Mathur et al. 2001, 1549). Therefore, the hydrogel produced by Device 2 can serve as a compatible implant within the environment of the chest cavity.

Chapter 4:

Concluding Remarks

Concluding Remarks

The design of a novel hydrogel barrier for the prevention of postsurgical cardiac adhesions is an important step in solving a relevant clinical problem. The issue of adhesive tissue formation affects a significant number of patients undergoing cardiovascular procedures, particularly those that must contend with follow-up surgeries years later. This is part of a healing response due to the entry of blood and healing factors into the damaged region of the heart's surface, which develop to form fibrous tissue that must be carefully dissected during reentry to the heart to avoid further complications (Cannata et al. 2013, 1818–19). Previous research into this problem has led to the development of the Ald-AO-DOPA hydrogel, a PEG-based material that has previously been validated through *in vivo* testing in murine models. While this trial demonstrated that the proposed material is indeed capable of preventing adhesions after injury, additional testing is required in order to properly implement it as a medical device. Two additional facets to this project that have been addressed by this study are the biocompatibility of the gel and the method of delivery used to apply the material to the heart during surgery.

The biocompatibility of a novel implantable substance is an important criterion for the transition of this hydrogel to a clinical setting. The results of this study in Chapter 2 have clearly shown that this issue is closely linked with the chemical formulation of the Ald-AO-DOPA gel and the relative amounts of dopamine-modified polymer used. While the earlier Ald-AO gel has been shown to be cytocompatible, the incorporation of 8-arm PEG-DOPA required further testing due to the known toxicity of excess dopamine, despite its role in promoting superior mechanical properties and better retention on the tissue surface (Grover et al. 2015, 1327). The oxidation of dopamine functional groups is necessary to obtain these properties, due to the formation of Schiff bases with the both PEG-AO and surface proteins on the anterior face of the

heart (Yang et al. 2016, 2). As a functional group bonded to a larger polymer network, dopamine is capable of creating an environment of oxidative stress *in vitro* primarily through the generation of H_2O_2. Through spectrophotometric assays, we have shown that the concentration of this ROS in culture lies in the range from 0.3 mM to 0.4 mM after incubation with both PEG-DOPA and the Ald-AO-DOPA gel. These results show that the stress is a direct result of the dopamine-functionalized component alone, as the levels of ROS seen are not present in cell culture samples incubated with PEG-Ald, PEG-AO or Ald-AO gel. The hazardous effects of dopamine oxidation can be rectified by the addition of GSH at a biologically relevant concentration, which is known to combat dopamine oxidation products directly (Segura-Aguilar et al. 2014, 901–2). Since H_2O_2 is the main stressor in the cases of cell death seen here, however, GSH could potentially be replaced by another antioxidant seen *in vivo* such as the enzyme catalase, which is known to reduce this peroxide specifically (Clement et al. 2002, 419).

The difficulty of evaluating material biocompatibility *in vitro* arises due to the fact that the testing environment does not replicate the conditions seen in a complete living system. This is demonstrated by the discrepancy observed when comparing the cytotoxic response of fibroblasts to dopamine-functionalized polymers and the lack of an adverse response seen during *in vivo* murine trials. The use of biological antioxidants such as GSH to maintain viability *in vitro* more closely mimics the factors affecting the *in vivo* response to the gel, due to the ubiquitous nature of this antioxidant in the body (Clement et al. 2002, 418–19). This indicates that the detrimental effects of dopamine caused by the presence of either PEG-DOPA or the Ald-AO-DOPA hydrogel are exclusive to cell culture testing.

One additional aspect of the *in vivo* condition that cannot be accounted for in the experiments proposed here is clearance of the material from the implant site over time. As a PEG-

based hydrogel, the anti-adhesion barrier possesses unique degradation kinetics that determine its rate of removal from the chest cavity over time. Previous work by Fujita et al. studying retention of the material to biopsy samples taken from heart tissue has shown that the Ald-AO-DOPA gel experiences a "burst release" of polymeric components over approximately the first 24 hours. As a result, it seems likely that normal fluid flux within the body would remove both the source and products of oxidative stress to would further diminish hazards affecting the tissue. In order to better simulate this process, one could consider using an *in vitro* method that can utilize fluid dynamics in order to simulate the effects of clearance during an incubation period. One potential solution is the use of microfluidics to mimic specific *in vivo* fluid flow rates in the presence of cultured cells in a controlled environment. A similar concept is seen in ongoing research involving organ-on-a-chip devices, which are largely studied for their potential applications in drug testing and discovery (Esch, Bahinski, and Huh 2015, 251). While this technology is still in development, the principles used could also be employed to evaluate the effects of polymer removal during degradation over time in a way that is more representative of normal bodily processes.

Different spraying techniques were considered prior to finalizing Design 2 as discussed here. A number of these methods deal specifically with materials made up of multiple polymer components that have been devised for non-biomedical applications such as the spray-coating of solar panels. This is typically accomplished using separate computer-assisted spray systems programmed to deposit each solution in succession onto the same region of a given surface (Chen et al. 2010, 4745). Other schematics, however, have implemented impinging "cones" of spray that intersect to simultaneously deliver equal amounts of material to the same point. This has been achieved by arranging two nozzles at an angle so that both the trajectories of each spray meet at a certain distance when sprayed, achieving complete overlap (Dohmann 1998, 342).

Coupled with the breakup of liquid into fine droplets by nozzle atomization, this type of delivery can produce a 1:1 mixture of each gel component on a given surface.

Developing a computer-aided simulation is a useful tool in developing a device that incorporates both gas and liquid flow. In the case of a fine air-driven spray, this can best be described by the discrete phase model, which approximates liquid droplets as a large collection of solid particles (ANSYS Inc. 2016, 381). Within a defined outlet opposite the source of spray separated into three equal regions, both devices demonstrate the greatest amount of deposition in the center of the area, with Design 2 more closely achieving the desired 1:1 ratio. The efficacy of this iteration is proven in physical testing of the device, as equal mixing of two distinct solutions is verified by absorbance measurements compared to a standard solution. Design 2 also achieves the formation of a working hydrogel using the formulation of the Ald-AO-DOPA material, as verified by the presence of oxime bonds identified through FTIR spectroscopy. Rheological studies of the hydrogel formed by this method indicate that the barrier produced experiences a similar evolution of the storage modulus over time compared to that observed in hydrogels formed by pipette as determined by Fujita et al. While a favorable distribution of droplets was predicted during steady-state simulations of Design 1 and oxime bond presence in the formed gel was confirmed by FTIR spectroscopy, this iteration did not adequately produce a 1:1 mixture of substitute solutions during physical testing, as evidenced by spectrophotometric data. Therefore, it can be concluded that Design 2 represents a more effective delivery method for future studies.

Additional work can be done to further validate this prototype as a reliable medical device for hydrogel implantation. Material retention assays were previously performed *ex vivo* by Fujita et al. in order to determine the amount of material lost from the tissue surface days after application. During these trials, the Ald-AO-DOPA material demonstrated superior retention to

the heart after an 8 day trial period relative to Ald-AO hydrogel samples. The material used in both groups of this original test was added in known volumes via pipette to the anterior faces of biopsies taken from the heart surface. This test would be beneficial to the development of a new delivery method by assessing the retention properties of the gel formed by this device in relation to proven techniques. Due to slight differences in volume when spraying across an area, this procedure would be slightly modified by spraying the entire anterior surface of the heart such that a layer of either Ald-AO or Ald-AO-DOPA is formed before subsequently separating the tissue and intact gels into equally sized pieces. In this way, a better understanding of material retention and degradation kinetics, and their relationship with the method of delivery used, can be determined.

After evaluating both the mechanical and retention properties of the hydrogel created by a spray-based technique, Design 2 could then be incorporated into a large animal study for adhesion prevention using the Ald-AO-DOPA hydrogel. While this same trial was not successful when using Design 1 for delivery, it seems likely that the lack of 1:1 mixing was a contributing factor to this outcome. Preliminary testing of Design 2, however, has shown promising results that indicate a two-spray system applied in this way can create a barrier that retains the chemical and mechanical properties of those delivered by other means. By ultimately using this design in a scenario that is more representative of the clinical environment, the delivery method used here can be further validated as a novel medical device.

The design of a novel synthetic barrier to prevent the formation of postsurgical adhesions is a task with many different components that must be considered to properly evaluate and implement this hydrogel during clinical procedures. By assessing the reactivity of the material under experimental conditions, this study addresses the potential biological effects of the Ald-

AO-DOPA gel while also providing evidence of its biocompatibility *in vitro*. Additionally, by considering the established mechanical and chemical properties of the crosslinked polymer network, a practical means of distributing the modified hydrogel across a tissue surface can be designed. In this way, this type of implantable device can be substantiated as a solution to a significant medical problem.

References

ANSYS Inc. 2016. “ANSYS Fluent Theory Guide.” *ANSYS Inc., USA* 15317 (August): 724–46. https://doi.org/10.1016/0140-3664(87)90311-2.

Bisaglia, Marco, Stefano Mammi, and Luigi Bubacco. 2007. “Kinetic and Structural Analysis of the Early Oxidation Products of Dopamine: Analysis of the Interactions with Alpha-Synuclein.” *Journal of Biological Chemistry* 282 (21): 15597–605.

Cannata, Aldo, Duccio Petrella, Claudio Francesco Russo, Giuseppe Bruschi, Pasquale Fratto, Marcello Gambacorta, and Luigi Martinelli. 2013. “Postsurgical Intrapericardial Adhesions: Mechanisms of Formation and Prevention.” *The Annals of Thoracic Surgery* 95 (5): 1818–26. https://doi.org/10.1016/j.athoracsur.2012.11.020.

Carr, R T, and S L Kotha. 1995. “Separation Surfaces for Laminar Flow in Branching Tubes--Effect of Reynolds Number and Geometry.” *Journal of Biomechanical Engineering* 117 (4): 442–47. https://doi.org/10.1115/1.2794205.

Chaurasia, Shyam S., Ravi Champakalakshmi, Romesh I. Angunawela, Donald T. Tan, and Jodhbir S. Mehta. 2012. “Optimization of Fibrin Glue Spray Systems for Ophthalmic Surgery.” *Translational Vision Science & Technology* 1 (2): 2. https://doi.org/10.1167/tvst.1.2.2.

Chen, Li-Min, Ziruo Hong, Wei Lek Kwan, Cheng-Hsueh Lu, Yi-Feng Lai, Bao Lei, Chuan-Pu Liu, and Yang Yang. 2010. “Multi-Source/Component Spray Coating for Polymer Solar Cells.” *ACS Nano* 4 (8): 4744–52. https://doi.org/10.1021/nn901758p.

Choi, Hong Y, Jin H Song, Dong K Park, and Gregory M Ross. 2000. “The Effects of Ascorbic Acid on Dopamine-Induced Death of PC12 Cells Are Dependent on Exposure Kinetics.” *Neuroscience Letters* 296 (2–3): 81–84. https://doi.org/10.1016/S0304-3940(00)01647-5.

Clement, Marie Véronique, Lee Hua Long, Jeyakumar Ramalingam, and Barry Halliwell. 2002. “The Cytotoxicity of Dopamine May Be an Artefact of Cell Culture.” *Journal of Neurochemistry* 81 (3): 414–21. https://doi.org/10.1046/j.1471-4159.2002.00802.x.

Dohmann, By Joachim. 1998. “Dispersion and Coagulation of Droplets in Intersecting Sprays” 21: 341–45.

Domínguez-Rebolledo, Á, F. Martínez-Pastor, M. R. Fernández-Santos, E. Del Olmo, A. Bisbal, J. L. Ros-Santaella, and J. J. Garde. 2010. “Comparison of the TBARS Assay and BODIPY C11 Probes for Assessing Lipid Peroxidation in Red Deer Spermatozoa.” *Reproduction in Domestic Animals* 45 (6): 360–68. https://doi.org/10.1111/j.1439-0531.2009.01578.x.

Dust, Julian M., Zhi Hao Fang, and J. Milton Harris. 1990. “Proton NMR Characterization of Poly(Ethylene Glycols) and Derivatives.” *Macromolecules* 23 (16): 3742–46. https://doi.org/10.1021/ma00218a005.

Ebner, F. M., A. Paul, J. Peters, and M. Hartmann. 2011. “Venous Air Embolism and Intracardiac Thrombus after Pressurized Fibrin Glue during Liver Surgery.” *British Journal of Anaesthesia* 106 (2): 180–82. https://doi.org/10.1093/bja/aeq336.

Esch, Eric W., Anthony Bahinski, and Dongeun Huh. 2015. “Organs-on-Chips at the Frontiers of Drug Discovery.” *Nature Reviews Drug Discovery* 14 (4): 248–60. https://doi.org/10.1038/nrd4539.

Fujita, Masaki, Gina Policastro, Austin Burdick, Jessica Ungerleider, Rebecca L. Braden, Diane Huang, Kent Osborn, Jeffery Omens, Michael Madani, and Karen Christman. 2018. “Preventing Post-Surgical Cardiac Adhesions with DOPA-Functionalized Oxime Hydrogel.”

Griffith, David T. 2016. *Basic Principles and Calculations in Process Technology*.

Grover, Gregory N., Rebecca L. Braden, and Karen L. Christman. 2013. “Oxime Cross-Linked Injectable Hydrogels for Catheter Delivery.” *Advanced Materials* 25 (21): 2937–42. https://doi.org/10.1002/adma.201205234.

Grover, Gregory N., Julian Garcia, Mary M. Nguyen, Matthew Zanotelli, Michael M. Madani, and Karen L. Christman. 2015. “Binding of Anticell Adhesive Oxime-Crosslinked PEG Hydrogels to Cardiac Tissues.” *Advanced Healthcare Materials* 4 (9): 1327–31. https://doi.org/10.1002/adhm.201500167.

Image-it. 2012. “Image-IT ® Lipid Peroxidation Kit,” 1–6.

ISO 15686-5. 2008. “International Standard” 2005: 22674. https://doi.org/10.5594/J09750.

Jacob, Matthias, Daniel Chappell, and Bernhard F. Becker. 2016. “Regulation of Blood Flow and Volume Exchange across the Microcirculation.” *Critical Care* 20 (1): 1–13. https://doi.org/10.1186/s13054-016-1485-0.

Joshi, Anand A, Abhijit J Chaudhari, Changqing Li, Joyita Dutta, Simon R Cherry, David W Shattuck, Arthur W Toga, and Richard M Leahy. 2011. “Design, Modeling, Fabrication, and Evaluation of the Air Amplifier for Improved Detection of Biomolecules by Electrospray Ionization Mass Spectrometry” 55 (20): 6197–6214. https://doi.org/10.1088/0031-9155/55/20/011.DigiWarp.

Liu, Yuan, Hao Meng, Shari Konst, Ryan Sarmiento, Rupak Rajachar, and Bruce P. Lee. 2014. “Injectable Dopamine-Modified Poly(Ethylene Glycol) Nanocomposite Hydrogel with Enhanced Adhesive Property and Bioactivity.” *ACS Applied Materials and Interfaces* 6 (19): 16982–92. https://doi.org/10.1021/am504566v.

Mathur, Anshu B., Amy M. Collinsworth, William M. Reichert, William E. Kraus, and George A. Truskey. 2001. “Endothelial, Cardiac Muscle and Skeletal Muscle Exhibit Different Viscous and Elastic Properties as Determined by Atomic Force Microscopy.” *Journal of Biomechanics* 34 (12): 1545–53. https://doi.org/10.1016/S0021-9290(01)00149-X.

Michelet, F., R. Gueguen, P. Leroy, M. Wellman, A. Nicolas, and G. Siest. 1995. “Blood and Plasma Glutathione Measured in Healthy Subjects by HPLC: Relation to Sex, Aging, Biological Variables, and Life Habits.” *Clinical Chemistry* 41 (10): 1509–17. https://doi.org/ .

Miller, P.C.H, and M.C Butler Ellis. 2000. “Effects of Formulation on Spray Nozzle Performance for Applications from Ground-Based Boom Sprayers.” *Crop Protection* 19 (8–10): 609–15. https://doi.org/10.1016/S0261-2194(00)00080-6.

Munson, Bruce, Donald Young, Theodore Okiishi, and Wade Huebsch. 2009. *Fundamentals of Fluid Mechanics*. Edited by Mark Owens. 6th ed. Wiley.

Pierce. 2012. “Pierce ® Quantitative Peroxide Assay Kits.” *Meridian* 0747 (815).

Segura-Aguilar, Juan, Irmgard Paris, Patricia Muñoz, Emanuele Ferrari, Luigi Zecca, and Fabio A. Zucca. 2014. “Protective and Toxic Roles of Dopamine in Parkinson’s Disease.” *Journal of Neurochemistry* 129 (6): 898–915. https://doi.org/10.1111/jnc.12686.

Spraying System Co. 2000. “Guidelines for Spray Nozzle Selection,” 4. www.spray.com.

Stepanenko, Dmitry A. 2007. “Modeling of Spraying with Time-Dependent Material Feed Rate.” *Applied Mathematical Modelling* 31 (11): 2564–76. https://doi.org/10.1016/J.APM.2006.10.005.

TISSEEL. 2017. “Highlights of Prescribing Information,” 1–9.

Whittemore, E.R., D.T. Loo, J.A. Watt, and C.W. Cotmans. 1995. “A Detailed Analysis of Hydrogen Peroxide-Induced Cell Death in Primary Neuronal Culture.” *Neuroscience* 67 (4): 921–32. https://doi.org/10.1016/0306-4522(95)00108-U.

Yang, Juan, Vittorio Saggiomo, Aldrik H. Velders, Martien A.Cohen Stuart, and Marleen Kamperman. 2016. “Reaction Pathways in Catechol/Primary Amine Mixtures: A Window on Crosslinking Chemistry.” *PLoS ONE* 11 (12): 1–17. https://doi.org/10.1371/journal.pone.0166490.